

Electrified magnetic catalysis in three-dimensional topological insulatorsE. V. Gorbar,^{1,2} V. A. Miransky,^{3,4} I. A. Shovkovy,⁵ and P. O. Sukhachov^{3,1}¹*Department of Physics, Taras Shevchenko National Kiev University, Kiev, 03680, Ukraine*²*Bogolyubov Institute for Theoretical Physics, Kiev, 03680, Ukraine*³*Department of Applied Mathematics, Western University, London, Ontario, Canada N6A 5B7*⁴*Department of Physics and Astronomy, Western University, London, Ontario, Canada N6A 3K7*⁵*College of Letters and Sciences, Arizona State University, Mesa, Arizona 85212, USA*

(Received 22 July 2016; published 22 September 2016)

The gap equations for the surface quasiparticle propagators in a slab of three-dimensional topological insulator in external electric and magnetic fields perpendicular to the slab surfaces are analyzed and solved. A different type of magnetic catalysis is revealed with the dynamical generation of *both* Haldane and Dirac gaps. Its characteristic feature manifests itself in the crucial role that the electric field plays in dynamical symmetry breaking and the generation of a Dirac gap in the slab. It is argued that, for a sufficiently large external electric field, the ground state of the system is a phase with a homogeneous surface charge density.

DOI: [10.1103/PhysRevB.94.115429](https://doi.org/10.1103/PhysRevB.94.115429)**I. INTRODUCTION**

Topological insulators (TIs) form a class of materials with unique properties, associated with a nontrivial topology of their quasiparticle band structure (for a review, see Refs. [1–4]). The key feature of two-dimensional (2D) and three-dimensional (3D) TIs is the existence of special gapless edge and surface states, respectively, while the bulk states of those materials are gapped. The hallmark property of the surface states is their topological protection. Mathematically, the nontrivial topological properties of time-reversal (TR) invariant TIs are generally described [5] by multiple copies of the Z_2 invariants found by Kane and Mele [6]. This implies that the energy band gap should close at the boundary between topological and trivial insulator (e.g., vacuum) giving rise to the occurrence of the gapless interface states and the celebrated bulk-boundary correspondence. The discovery of the Z_2 topology in TIs is an important breakthrough because it showed that nontrivial topology can be embedded in the band structure and that the presence of an external magnetic field is not mandatory for the realization of topological phases.

Another distinctive feature of the 3D TIs is a relativisticlike energy spectrum of the surface states, whose physical origin is related to a strong spin-orbit coupling [7]. Indeed, the surface states on each of the surfaces are described by 2D massless Dirac fermions in an irreducible 2×2 representation, with a single Dirac point in the reciprocal space. For comparison, quasiparticles in graphene demonstrate similar properties, but have four inequivalent Dirac cones due to a spin and valley degeneracy [8] that makes certain aspects of their physics very different from those of the surface states in TIs. In our study below, we will concentrate only on the case of the strong 3D TIs whose surface states are protected by the topology of the bulk bands in combination with the TR symmetry. This leads to the locking of momenta and spin degrees of freedom and, consequently, to the formation of a helical Dirac (semi)metal state [7]. Such a state is characterized by the electron antilocalization and the absence of backscattering. The phenomenon of antilocalization has deep mathematical roots and is usually explained by an additional Berry's phase π that is acquired when an electron circles a Dirac point. From the

physical viewpoint, when scattering on an impurity, an electron must change its spin in order to preserve its chirality. Such a process is possible only in the case of magnetic impurities which break explicitly the TR symmetry.

Experimentally, a linear relativisticlike dispersion law of the surface states is observed in $\text{Bi}_{1-x}\text{Sb}_x$, Bi_2Se_3 , Bi_2Te_3 , Sb_2Te_3 , $\text{Bi}_2\text{Te}_2\text{Se}$, and other materials by using angle-resolved photoemission spectroscopy (ARPES) [7,9–12]. Furthermore, scanning tunneling microscopy and scanning tunneling spectroscopy provide additional information about the topological nature of the surface states, such as the quasiparticles' interference patterns around impurities and defects. The Fourier analysis of these patterns has shown that the backscattering between \mathbf{k} and $-\mathbf{k}$ is highly suppressed in $\text{Bi}_{1-x}\text{Sb}_x$ [13] and Bi_2Te_3 [14] in accord with the TR symmetry protection. The existence of an odd number of Dirac nodes leads to other exotic properties associated with surface states of TIs, e.g., an axion electromagnetic response [15], an unusual surface Hall conductance [16,17], etc.

It is well known that electrons confined to two dimensions can form numerous interaction-induced phases. By using numerical calculations, it was shown in Ref. [18] that it is energetically favorable for the 2D electron liquid in a weak magnetic field to form domains with empty and fully filled higher Landau levels. Depending on the number of Landau levels filled, the corresponding charge density wave (CDW) phase is realized with a “stripe” or “bubble” pattern. By using the simplest model of the surface states in a magnetic field with strong local repulsion and a long-range Coulomb interaction included perturbatively, it was suggested that a similar CDW phase with a “stripe” or “bubble” pattern can be also realized on the surface of 3D TIs for supercritical values of a local repulsion constant [19]. For subcritical local repulsion, the composite Fermi liquid (CFL) [20] phase is expected [19,21]. It is interesting that composite fermions in conventional 2D electron gas at half-filling were recently suggested to be massless Dirac (quasi)particles [22] similar to the surface quasiparticles of TIs. This result was also checked numerically in Ref. [23], where it was shown that at the half-filling the particle-hole symmetry for composite fermions plays the same role as the TR symmetry for the

2D Dirac fermions and, consequently, the backscattering off symmetry-preserving impurities is also forbidden.

The influence of an external electric field on the exciton condensation in thin films of TIs was studied in Refs. [24,25], where it was shown that the electron condensate effectively joins the surfaces of a thin film and leads to the formation of a pairing gap. However, this is important only in thin ($l_z \lesssim 8$ nm) films of TIs and can be ignored in sufficiently thick slabs [26]. The exciton condensate exhibits unusual properties including a stable zero mode and a fractional charge $\pm e/2$ carried by a singly quantized vortex in the exciton condensate [24]. The dynamical gap generation in a simple model of TIs was also considered in Ref. [27].

Just like a magnetic field, an external electric field may play an important role in the dynamics of the surface states in a 3D TI slab. In this paper, we study the dynamical gap generation and the phase diagram of a TI slab placed in external magnetic and electric fields perpendicular to the slab surfaces. (Note that the case of the parallel fields is rather trivial. While a parallel magnetic field does not affect the orbital motion, a parallel electric field produces a current on the surface.) We argue that a uniform phase with both dynamically generated Dirac and Haldane gaps is realized in sufficiently strong (weak) electric (magnetic) fields. Although the explicit calculations performed in this paper use the model parameters suitable for Bi_2Se_3 , the main qualitative conclusions should be valid for all similar TIs.

The paper is organized as follows. The effective Hamiltonian of the surface states in the simplest model of a topological insulator with short- and long-range interactions is described in Sec. II. The set of gap equations at finite temperature is derived in Sec. III and its solutions in electric and magnetic fields are obtained numerically in Sec. IV. The qualitative description of the inhomogeneous phase with two stripes is given in Sec. V. The main results are discussed and summarized in Secs. VI and VII, respectively.

For convenience, throughout the paper, we set $\hbar = c = 1$.

II. MODEL

By projecting the 3D bulk Hamiltonian onto the subspace of surface states (see Refs. [1,28] for a detailed consideration), the following effective Hamiltonian for the top surface of a 3D TI is obtained [1,10,28,29]:

$$\begin{aligned} \mathcal{H}_{\text{top surf}}(\mathbf{k}) &= C + v_F(\boldsymbol{\sigma} \times \mathbf{k})_z + \mathcal{O}(\mathbf{k}^2) \\ &= C + \begin{pmatrix} 0 & v_F(ik_x + k_y) \\ v_F(-ik_x + k_y) & 0 \end{pmatrix} + \mathcal{O}(\mathbf{k}^2), \end{aligned} \quad (1)$$

where C is a constant, $\boldsymbol{\sigma} = (\sigma_x, \sigma_y)$ are the Pauli matrices, $v_F = 4.1 \text{ eV}\text{\AA} = 6.2 \times 10^5 \text{ m/s}$ is the Fermi velocity, and $\mathbf{k} = (k_x, k_y)$ is the surface momentum. The effective surface Hamiltonian for the bottom surface is obtained from the Hamiltonian of the top surface by the inversion $\mathbf{k} \rightarrow -\mathbf{k}$ (see Sec. III C in Ref. [1]). It is worth noting that the effective surface Hamiltonian is valid only at sufficiently small chemical potentials, when the bulk states are gapped. Therefore, the corresponding energy cutoff can be approximated by the bulk

band gap, i.e., $\Lambda \simeq \Delta_{\text{bulk}}$. In the case of Bi_2Se_3 , for example, $\Delta_{\text{bulk}} \approx 0.35 \text{ eV}$ [30,31].

The resulting model Hamiltonian, describing quasiparticle states on the top and bottom surfaces of the 3D TI in constant electric and magnetic fields applied perpendicular to the surfaces of the slab, is given by $H^{(0)} = H_+^{(0)} \oplus H_-^{(0)}$, where

$$\begin{aligned} H_\lambda^{(0)} &= \int d^2\mathbf{r} \psi_\lambda^\dagger(\mathbf{r}) \\ &\times \begin{pmatrix} m^{(0)} - \mu_\lambda^{(0)} & iv_F(\pi_x - i\pi_y) \\ -iv_F(\pi_x + i\pi_y) & -m^{(0)} - \mu_\lambda^{(0)} \end{pmatrix} \psi_\lambda(\mathbf{r}). \end{aligned} \quad (2)$$

Here, $\lambda = \pm$ denotes the top and bottom surfaces, respectively, $\mu_\lambda^{(0)}$ is the surface electrochemical potential, $\boldsymbol{\pi} \equiv -i\nabla + e\mathbf{A}$ is the canonical momentum, $\mathbf{A} = (0, Bx)$ is the vector potential that describes the constant magnetic field \mathbf{B} pointing in the z direction, and e is the electron charge. Note that in Eq. (2) we redefined the wave function on the bottom surface by replacing $\psi_- \rightarrow \sigma_z \psi_-$. As the notation suggests, the value of $\mu_\lambda^{(0)}$ may depend on the surface index λ . Indeed, this is quite natural in the model at hand since fixing charge densities on the top and bottom surfaces requires an introduction of the corresponding local electrochemical potentials. In view of a large surface g factor, $g_s = 18 \pm 4$ [32], the Zeeman splitting is important in TIs. This spin splitting is included in Hamiltonian (2) as the bare gap parameter $m^{(0)} = g_s \mu_B B/2$, where $\mu_B = 5.788 \times 10^{-5} \text{ eV/T}$ is the Bohr magneton.

Before proceeding with the analysis of the model, it is convenient to rewrite the model Hamiltonian (2) in terms of the Dirac matrices. It is well known that there are two irreducible representations of the Clifford-Dirac algebra in (2+1) dimensions, e.g., see Ref. [33]. One of them is

$$\gamma^0 = \sigma_z, \quad \gamma^1 = i\sigma_x, \quad \gamma^2 = i\sigma_y \quad (3)$$

and the other irreducible representation is obtained by changing $\gamma^\mu \rightarrow -\gamma^\mu$ with $\mu = 0, 1, 2$ in Eq. (3). In terms of the Dirac matrices (3), the free Hamiltonian (2) takes the following form:

$$H_\lambda^{(0)} = \int d^2\mathbf{r} \bar{\psi}_\lambda(\mathbf{r}) (-\mu_\lambda^{(0)} \gamma^0 + v_F(\boldsymbol{\pi} \cdot \boldsymbol{\gamma}) + m^{(0)}) \psi_\lambda(\mathbf{r}), \quad (4)$$

where $\bar{\psi}_\lambda(\mathbf{r}) = \psi_\lambda^\dagger(\mathbf{r})\gamma^0$. When an external electric field is applied perpendicularly to the surfaces of the TI slab, the gapless surface states will tend to completely screen the field out. Indeed, from a physics viewpoint, the TI slab is like a Faraday cage made of gapless (metallic) surface states enclosing a gapped (insulating) interior. This implies that there should be no electric field inside a (sufficiently thick) TI slab. Enforcing this condition allows one to determine the charge densities and electrochemical potentials on the surfaces. In terms of the charge densities on the top and bottom surfaces, one has

$$\rho_\lambda = \lambda \epsilon_0 \mathcal{E}, \quad (5)$$

where \mathcal{E} is the external electric field pointing in the z direction, $\epsilon_0 \approx 8.854 \times 10^{-12} \text{ F/m}$ is the permittivity of free space, and $2\epsilon_0 \mathcal{E}$ corresponds to the difference of the charge densities of the top and bottom surfaces needed to compensate the external electric field.

Under the parity transformation P in (2+1) dimensions, which changes the sign of a spatial coordinate, i.e., $(x, y) \rightarrow (-x, y)$, the two-component spinors transform as follows: $P\psi(t, x, y)P^{-1} = \sigma_x \psi(t, -x, y)$. Clearly, the last term in Hamiltonian (4) breaks parity, as well as the TR symmetry $T\psi(t, x, y)T^{-1} = \sigma_y \psi^*(-t, x, y)$. This mass term is known in the literature as the Haldane mass $\sum_\lambda m_H \bar{\psi}_\lambda \psi_\lambda$ [34]. A parity and TR invariant mass is also possible in the model with two irreducible representations. It is given by the Dirac mass term $\sum_\lambda m_D \lambda \bar{\psi}_\lambda \psi_\lambda$ with the parity transformation defined by $\psi_{\lambda=+1} \rightarrow \sigma_x \psi_{\lambda=-1}$ and $\psi_{\lambda=-1} \rightarrow \sigma_x \psi_{\lambda=+1}$. (Note that, in the TI slab model, this transformation interchanges the states on the different spatially separated surfaces.) While a Chern-Simons mass term for the gauge field is induced via one-loop polarization when the Haldane mass is present, the Chern-Simons term is absent in the case of the Dirac mass. The spontaneous breaking of parity in (2 + 1)-dimensional QED was studied in Ref. [35].

In this study, the model interaction Hamiltonian H_{int} includes both a long-range Coulomb and a short-range local four-fermion interaction

$$H_{\text{int}} = \frac{e^2}{8\pi\epsilon_0\kappa_{\text{surf}}} \int d^2\mathbf{r} d^2\mathbf{r}' \frac{\Psi^\dagger(\mathbf{r})\Psi(\mathbf{r})\Psi^\dagger(\mathbf{r}')\Psi(\mathbf{r}')}{|\mathbf{r} - \mathbf{r}'|} + \frac{G_{\text{int}}}{2} \int d^2\mathbf{r} \Psi^\dagger(\mathbf{r})\Psi(\mathbf{r})\Psi^\dagger(\mathbf{r})\Psi(\mathbf{r}), \quad (6)$$

where $\Psi(\mathbf{r}) = (\psi_{\lambda=+1}(\mathbf{r}), \psi_{\lambda=-1}(\mathbf{r}))^T$. The first term in H_{int} describes the long-range Coulomb interaction and takes into account the effective surface dielectric constant $\kappa_{\text{surf}} = (1 + \kappa_{\text{bulk}})/2 \approx 56$, where the bulk dielectric constant $\kappa_{\text{bulk}} \approx 113$ for Bi_2Se_3 [36]. The second term captures the onsite local repulsion, parametrized by the dimensionful coupling constant G_{int} . In view of the large bulk dielectric constant and assuming a large slab thickness, we neglect the intersurface interaction and the possible formation of an intersurface exciton condensate [24,25]. Thus, the full Hamiltonian of our model is given by the sum of the free and interaction Hamiltonians in Eqs. (4) and (6).

III. GAP EQUATIONS

In this section, we study the gap generation in the effective model of a sufficiently thick TI slab described in the previous section. The inverse free surface fermion propagator is given by

$$iS_\lambda^{-1}(u, u') = [(i\partial_t + \mu_\lambda^{(0)})\gamma^0 - v_F(\boldsymbol{\pi} \cdot \boldsymbol{\gamma}) - m^{(0)}]\delta^3(u - u'), \quad (7)$$

where $u = (t, \mathbf{r})$ denotes a space-time coordinate. By using this as a guide, we assume the following rather general ansatz for the inverse full surface fermion propagator:

$$iG_\lambda^{-1}(u, u') = [(i\partial_t + \mu_\lambda)\gamma^0 - v_F(\boldsymbol{\pi} \cdot \boldsymbol{\gamma}) - m_\lambda]\delta^3(u - u'), \quad (8)$$

where m_λ is a dynamically generated gap (mass) which, in general, includes both Haldane and Dirac gaps and μ_λ denotes the dynamical electrochemical potential. Note that all dynamical parameters in the full propagator are assumed to

be functions of $(\boldsymbol{\pi} \cdot \boldsymbol{\gamma})^2 l^2$, where $l = 1/\sqrt{|eB|}$ is the magnetic length. Therefore, in the end, they all depend on the Landau level index n .

Because of the long-range interaction, in principle, the renormalization of the wave function should be included in the full propagator (8). This can be formally done by replacing the Fermi velocity v_F with a dynamical function F_λ . It is well justified, however, to neglect the renormalization of the Fermi velocity and replace it with v_F . Indeed, even in the case of graphene with an unscreened Coulomb interaction, the renormalized Fermi velocity is generically 10% to 30% larger than the corresponding bare value v_F [37–39]. Because of a much larger surface dielectric constant and, consequently, a much smaller coupling constant, the Coulomb interaction will play a minor role in the Fermi velocity renormalization and, as we will show below, in the generation of dynamical gaps in TIs.

In order to represent the inverse propagator in the form of a Landau-level expansion, we use the following complete set of eigenstates (for details, see Appendix A in Ref. [39]):

$$\psi_{n, k_y}(\mathbf{r}) = \frac{1}{\sqrt{2^{n+1}\pi l n!}} H_n\left(k_y l + \frac{x}{l}\right) e^{-\frac{1}{2l^2}(x+k_y l)^2} e^{i s_B k_y y}, \quad (9)$$

where $H_n(x)$ are the Hermite polynomials and $s_B = \text{sign}(eB)$. By making use of the results in Appendix A, we derive the following inverse fermion propagators in the mixed frequency-momentum representation:

$$S_\lambda^{-1}(\omega, \mathbf{r}, \mathbf{r}') = e^{i\Phi(\mathbf{r}, \mathbf{r}')} \tilde{S}_\lambda^{-1}(\omega, \mathbf{r} - \mathbf{r}'), \quad (10)$$

$$G_\lambda^{-1}(\omega, \mathbf{r}, \mathbf{r}') = e^{i\Phi(\mathbf{r}, \mathbf{r}')} \tilde{G}_\lambda^{-1}(\omega, \mathbf{r} - \mathbf{r}'). \quad (11)$$

Here $\Phi(\mathbf{r}, \mathbf{r}') = -eB(x + x')(y - y')/2$ is the famous Schwinger phase and the translation-invariant parts of the inverse propagators are given by

$$iS_\lambda^{-1}(\omega, \mathbf{r} - \mathbf{r}') = \frac{e^{-\eta/2}}{2\pi l^2} \sum_{n=0}^{\infty} \left\{ s_B(\omega + \mu_\lambda^{(0)}) [P_+ L_{n-1}(\eta) - P_- L_n(\eta)] - m^{(0)} [P_+ L_{n-1}(\eta) + P_- L_n(\eta)] - \frac{i}{l^2} v_F (\boldsymbol{\gamma} \cdot \mathbf{r}) L_{n-1}^1(\eta) \right\}, \quad (12)$$

$$iG_\lambda^{-1}(\omega, \mathbf{r} - \mathbf{r}') = \frac{e^{-\eta/2}}{2\pi l^2} \sum_{n=0}^{\infty} \left\{ s_B(\omega + \mu_{n, \lambda}) [P_+ L_{n-1}(\eta) - P_- L_n(\eta)] - m_{n, \lambda} [P_+ L_{n-1}(\eta) + P_- L_n(\eta)] - \frac{i}{l^2} v_F (\boldsymbol{\gamma} \cdot \mathbf{r}) L_{n-1}^1(\eta) \right\}, \quad (13)$$

where $P_\pm = (1 \pm s_B \gamma^0)/2$, $\eta = (\mathbf{r} - \mathbf{r}')^2 / (2l^2)$, and $L_n^j(x)$ are the generalized Laguerre polynomials (by definition $L_n \equiv L_n^0$).

In order to study the dynamical gap generation, we utilize the Baym-Kadanoff (BK) formalism [40], which leads to a self-consistent Schwinger-Dyson equation for the fermion propagator. In contrast to a perturbative analysis, the BK formalism can capture nonperturbative effects such as spontaneous symmetry breaking. To leading order in coupling, the BK effective action in the model under consideration is given by Eq. (B7) in Appendix B. In view of the geometry

of conducting states of our TI system, it should not be too surprising that the effective action (B7) has a form similar to that in bilayer graphene [compare with Eq. (9) in Ref. [41]].

The extremum of the effective action $\frac{\delta\Gamma(G)}{\delta G_\lambda} = 0$ defines the following Schwinger-Dyson equation for the full fermion propagator (for details, see Appendix B):

$$iG_\lambda^{-1}(u, u') = iS_\lambda^{-1}(u, u') - e^2 \gamma^0 G_\lambda(u, u') \gamma^0 D(u' - u) - G_{\text{int}} \{ \gamma^0 G_\lambda(u, u) \gamma^0 - \gamma^0 \text{tr}[\gamma^0 G_\lambda(u, u)] \} \delta^3(u - u'), \quad (14)$$

where the trace in the last term is taken over the spinor indices and the Hartree term due to the Coulomb interaction is absent. This is justified because of the overall neutrality of the sample, i.e.,

$$Q_b - e \sum_{\lambda=\pm} \text{tr}[\gamma^0 G_\lambda(u, u)] = 0, \quad (15)$$

where Q_b denotes the background charge due to the external gates. We note, however, that it does not make sense to drop the Hartree-type term due to the contact interaction. Therefore, the corresponding term is kept in curly brackets in Eq. (14).

The propagator mediating the Coulomb interaction is denoted by $D(u)$. Its explicit expression is given by

$$D(u) = \int \frac{d\omega d^2\mathbf{k}}{(2\pi)^3} D(\omega, \mathbf{k}) e^{-i\omega t + i\mathbf{k}\cdot\mathbf{r}} \approx \delta(t) \frac{1}{4\pi\epsilon_0\kappa_{\text{surf}}} \int \frac{dk}{2\pi} \frac{kJ_0(kr)}{k + \Pi(0, k)}, \quad (16)$$

where $J_0(x)$ is the Bessel function. In the last expression, we neglected the dependence of the polarization function $\Pi(\omega, k)$ on ω , which corresponds to an instantaneous approximation. Such an approximation may be reasonable for the TI surfaces, where charge carriers propagate much slower than the speed of light and, thus, the retardation effects are negligible. It is worth noting, however, that the instantaneous approximation has a tendency to underestimate the strength of the Coulomb interaction [42].

Just like the inverse propagators in Eqs. (10) and (11), the propagators themselves have the same Schwinger phase. The full propagator, in particular, takes the following explicit form:

$$G_\lambda(\omega, \mathbf{r}, \mathbf{r}') = e^{i\Phi(\mathbf{r}, \mathbf{r}')} \tilde{G}_\lambda(\omega, \mathbf{r} - \mathbf{r}'), \quad (17)$$

$$\tilde{G}_\lambda(\omega, \mathbf{r} - \mathbf{r}') = \frac{e^{-\eta/2}}{2\pi l^2} \sum_{n=0}^{\infty} \left\{ \frac{s_B(\omega + \mu_{n,\lambda}) [L_{n-1}(\eta)P_+ - L_n(\eta)P_-]}{[\omega + \mu_{n,\lambda} + i0 \text{sign}(\omega)]^2 - M_n^2} + \frac{m_{n,\lambda} [L_{n-1}(\eta)P_+ + L_n(\eta)P_-] - i \frac{v_F}{l^2} L_{n-1}(\eta) [\boldsymbol{\gamma} \cdot (\mathbf{r} - \mathbf{r}')] }{[\omega + \mu_{n,\lambda} + i0 \text{sign}(\omega)]^2 - M_n^2} \right\}, \quad (18)$$

where $M_n = \sqrt{(m_{n,\lambda})^2 + \epsilon_B^2 n}$ and $\epsilon_B = \sqrt{2v_F^2 |eB|}$ is the Landau energy scale. The inverse and full fermion propagators at finite temperature are easily obtained through the standard replacement $\omega \rightarrow i\omega_m = i\pi T(2m' + 1)$.

By factorizing the Schwinger phase on both sides of Eq. (14), we arrive at the following gap equation for the translation-invariant part of the full propagator:

$$i\tilde{G}_\lambda^{-1}(\omega, \mathbf{r}) = i\tilde{S}_\lambda^{-1}(\omega, \mathbf{r}) - \alpha v_F \int \frac{d\Omega dk}{2\pi} \frac{kJ_0(kr)}{k + \Pi(0, k)} \gamma^0 \tilde{G}_\lambda(\Omega, \mathbf{r}) \gamma^0 - G_{\text{int}} \int \frac{d\Omega}{2\pi} \delta^2(\mathbf{r}) \{ \gamma^0 \tilde{G}_\lambda(\Omega, \mathbf{r}) \gamma^0 - \gamma^0 \text{tr}[\gamma^0 \tilde{G}_\lambda(\Omega, \mathbf{r})] \}. \quad (19)$$

Here, we introduced the following notation: $\alpha = e^2/(4\pi\epsilon_0 v_F \kappa_{\text{surf}})$. In the case of Bi_2Se_3 , in particular, $\alpha \approx 0.062$. Although it is hard to estimate G_{int} reliably, its origin is the Coulomb repulsion on distance scales comparable to the lattice spacing. Thus, it may be reasonable to use the following approximate model value:

$$G_{\text{int}} = \frac{\alpha v_F^2 \kappa_{\text{surf}}}{\Delta_{\text{bulk}}} \approx 168.7 \text{ eV}\text{\AA}^2, \quad (20)$$

where the factor κ_{surf} was introduced in order to compensate for polarization effects in the definition of α . Indeed, polarization effects should be negligible at small distances. It is worth noting that the corresponding dimensionless constant

$$g_{\text{int}} = \frac{G_{\text{int}} \Delta_{\text{bulk}}}{8\sqrt{2\pi} v_F^2} \approx 0.18 \quad (21)$$

is rather small. In fact, it is an order of magnitude smaller than the critical value $g_{cr} = \sqrt{\pi}$ needed for generating a gap in a (2+1)-dimensional model in the absence of a magnetic field [43]. Because of this and because of the strong suppression of the Coulomb interaction by the large dielectric constant, no dynamical generation of a gap is expected in such a TI material in the absence of an external magnetic field. Consequently, the magnetic catalysis [43] will play a crucial role in the generation of dynamical gaps in TIs. (For a recent review on magnetic catalysis, see Ref. [44].)

By using the explicit form of the fermion propagator (18) on the right-hand side of Eq. (19), we can easily calculate the integral over Ω (or the sum over the Matsubara frequency at nonzero temperature, see Appendix A 2). Afterwards, by multiplying both

sides of the gap equation (19) by $e^{-\eta/2}L_{n'}(\eta)$ or $e^{-\eta/2}(\boldsymbol{\gamma} \cdot \mathbf{r})L_{n'}^1(\eta)$ and then integrating over \mathbf{r} , the complete set of equations for the dynamical parameters can be straightforwardly obtained. In particular, the gap equations for the lowest Landau level (LLL) parameters are given by

$$\begin{aligned} \Delta_{\text{eff},\lambda} = & \mu_{\lambda}^{(0)} + s_B m^{(0)} + \alpha \frac{v_F}{2l} \left\{ \mathcal{K}_{0,0}^{(0)} [1 - 2n_F(\Delta_{\text{eff},\lambda})] - \sum_{n'=1}^{\infty} \mathcal{K}_{n',0}^{(0)} \left[n_F(M_{n'} + \mu_{n',\lambda}) - n_F(M_{n'} - \mu_{n',\lambda}) \right. \right. \\ & \left. \left. - s_B m_{n',\lambda} \frac{1 - n_F(M_{n'} + \mu_{n',\lambda}) - n_F(M_{n'} - \mu_{n',\lambda})}{M_{n'}} \right] \right\} + \frac{G_{\text{int}}}{4\pi l^2} \left\{ \sum_{n'=1}^{\infty} [n_F(M_{n'} + \mu_{n',\lambda}) - n_F(M_{n'} - \mu_{n',\lambda})] \right. \\ & \left. + \sum_{n'=1}^{\infty} s_B m_{n',\lambda} \frac{1 - n_F(M_{n'} + \mu_{n',\lambda}) - n_F(M_{n'} - \mu_{n',\lambda})}{M_{n'}} \right\}, \end{aligned} \quad (22)$$

where $n_F(x) = 1/(e^{x/T} + 1)$ is the Fermi-Dirac distribution. Notice that we introduced an effective LLL electrochemical potential $\Delta_{\text{eff},\lambda} = \mu_{0,\lambda} + s_B m_{0,\lambda}$ because the LLL parameters $\mu_{0,\lambda}$ and $m_{0,\lambda}$ cannot be unambiguously defined separately and only their combination $\Delta_{\text{eff},\lambda}$ has a well-defined physical meaning [45,46]. Similarly, the equations for the dynamical parameters associated with higher Landau levels read as

$$\begin{aligned} m_{n,\lambda} = & m^{(0)} + s_B \alpha \frac{v_F}{4l} \left\{ \mathcal{K}_{0,n}^{(0)} [1 - 2n_F(\Delta_{\text{eff},\lambda})] + \sum_{n'=1}^{\infty} \mathcal{K}_{n'-1,n-1}^{(0)} \left[n_F(M_{n'} + \mu_{n',\lambda}) - n_F(M_{n'} - \mu_{n',\lambda}) \right. \right. \\ & \left. \left. + s_B m_{n',\lambda} \frac{1 - n_F(M_{n'} + \mu_{n',\lambda}) - n_F(M_{n'} - \mu_{n',\lambda})}{M_{n'}} \right] \right. \\ & \left. - \sum_{n'=1}^{\infty} \mathcal{K}_{n',n}^{(0)} \left[n_F(M_{n'} + \mu_{n',\lambda}) - n_F(M_{n'} - \mu_{n',\lambda}) - s_B m_{n',\lambda} \frac{1 - n_F(M_{n'} + \mu_{n',\lambda}) - n_F(M_{n'} - \mu_{n',\lambda})}{M_{n'}} \right] \right\} \\ & + \frac{G_{\text{int}}}{8\pi l^2} \left\{ s_B [1 - 2n_F(\Delta_{\text{eff},\lambda})] + 2 \sum_{n'=1}^{\infty} m_{n',\lambda} \frac{1 - n_F(M_{n'} + \mu_{n',\lambda}) - n_F(M_{n'} - \mu_{n',\lambda})}{M_{n'}} \right\}, \end{aligned} \quad (23)$$

$$\begin{aligned} \mu_{n,\lambda} = & \mu_{\lambda}^{(0)} + \alpha \frac{v_F}{4l} \left\{ \mathcal{K}_{0,n}^{(0)} [1 - 2n_F(\Delta_{\text{eff},\lambda})] - \sum_{n'=1}^{\infty} \mathcal{K}_{n'-1,n-1}^{(0)} \left[n_F(M_{n'} + \mu_{n',\lambda}) - n_F(M_{n'} - \mu_{n',\lambda}) \right. \right. \\ & \left. \left. + s_B m_{n',\lambda} \frac{1 - n_F(M_{n'} + \mu_{n',\lambda}) - n_F(M_{n'} - \mu_{n',\lambda})}{M_{n'}} \right] - \sum_{n'=1}^{\infty} \mathcal{K}_{n',n}^{(0)} \left[n_F(M_{n'} + \mu_{n',\lambda}) - n_F(M_{n'} - \mu_{n',\lambda}) \right. \right. \\ & \left. \left. - s_B m_{n',\lambda} \frac{1 - n_F(M_{n'} + \mu_{n',\lambda}) - n_F(M_{n'} - \mu_{n',\lambda})}{M_{n'}} \right] \right\} \\ & - \frac{G_{\text{int}}}{8\pi l^2} \left\{ [1 - 2n_F(\Delta_{\text{eff},\lambda})] - 2 \sum_{n'=1}^{\infty} [n_F(M_{n'} + \mu_{n',\lambda}) - n_F(M_{n'} - \mu_{n',\lambda})] \right\}. \end{aligned} \quad (24)$$

The kernel coefficients $\mathcal{K}_{m,n}^{(0)}$ that capture the long-range interaction effects in the gap equations are defined in Eq. (C1). In this study, for simplicity, we neglect all screening effects, i.e., we set $\Pi(0,k) = 0$. Then, the numerical analysis greatly simplifies because the coefficients $\mathcal{K}_{m,n}^{(0)}$ can be calculated analytically [see Eq. (C3)].

In addition to the gap equation (19), the constraints for the surface charge densities in Eq. (5) should be also satisfied. In terms of the model parameters, the explicit form of the constraint reads as

$$-\frac{e}{4\pi l^2} \left\{ [1 - 2n_F(\Delta_{\text{eff},\lambda})] - 2 \sum_{n=1}^{\infty} [n_F(M_n + \mu_{n,\lambda}) - n_F(M_n - \mu_{n,\lambda})] \right\} = \lambda \epsilon_0 \mathcal{E}, \quad (25)$$

where we used the definition for the surface charge densities in terms of the fermion propagator, i.e., $\rho_{\lambda} = e \text{tr}[G_{\lambda}(u,u)\gamma^0]$. Because the surface charge density is fixed by the external electric field, the electrochemical potential $\mu_{\lambda}^{(0)}$ is not an independent parameter. It is determined together with the other dynamical parameters by solving the system of Eqs. (22)–(25).

IV. NUMERICAL RESULTS

In this section, we present our numerical solutions of gap equations (22)–(24), together with the constraint in Eq. (25). Before proceeding to the analysis, it is convenient to give the formal definition of the Dirac and Haldane gaps in the TI model at hand. While the original surface gaps $m_{n,+}$ and $m_{n,-}$ (with

$n \geq 1$) have a straightforward physical meaning, the symmetry properties of the ground state can be better understood in terms of Dirac and Haldane gaps, i.e.,

$$m_{n,D} = \frac{m_{n,+} - m_{n,-}}{2}, \quad m_{n,H} = \frac{m_{n,+} + m_{n,-}}{2}. \quad (26)$$

Strictly speaking, these gaps cannot be associated with the usual Dirac and Haldane masses in (2+1)-dimensional QED (see Ref. [33]) because m_{\pm} in TIs correspond to spatially separated surfaces. Since the free Hamiltonian (2) contains the bare Haldane gap $m^{(0)}$ due to the Zeeman interaction, it is also convenient to define the dynamical part of the total Haldane gap $\Delta m_{n,H} \equiv m_{n,H} - m^{(0)}$.

In order to provide an insight into relation (26) between m_{\pm} and Dirac and Haldane gaps, let us recall the reducible 4×4 representation for QED₂₊₁ considered in Ref. [33]:

$$\begin{aligned} \tilde{\gamma}^0 &= \begin{pmatrix} \gamma^0 & 0 \\ 0 & -\gamma^0 \end{pmatrix}, & \tilde{\gamma}^1 &= \begin{pmatrix} \gamma^1 & 0 \\ 0 & -\gamma^1 \end{pmatrix}, \\ \tilde{\gamma}^2 &= \begin{pmatrix} \gamma^2 & 0 \\ 0 & -\gamma^2 \end{pmatrix}. \end{aligned} \quad (27)$$

In this representation, in addition to the γ matrices in Eq. (27), there exist two other matrices

$$\tilde{\gamma}^3 = i \begin{pmatrix} 0 & 1 \\ 1 & 0 \end{pmatrix}, \quad \tilde{\gamma}^5 = i \begin{pmatrix} 0 & 1 \\ -1 & 0 \end{pmatrix}, \quad (28)$$

which anticommute with $\tilde{\gamma}^0$, $\tilde{\gamma}^1$, and $\tilde{\gamma}^2$. In terms of these 4×4 matrices, the existence of a U(2) symmetry in the model of a TI slab, defined by Eqs. (4) and (6), is transparent. The corresponding group generators are given by

$$1, \quad i\mathcal{R}_{\mu}\tilde{\gamma}^3, \quad \mathcal{R}_{\mu}\tilde{\gamma}^5, \quad \text{and} \quad \tilde{\gamma}^3\tilde{\gamma}^5, \quad (29)$$

where \mathcal{R}_{μ} is the operator which interchanges $\mu_{+}^{(0)} \leftrightarrow \mu_{-}^{(0)}$ in the low-energy free Hamiltonian (4). (Note that, in the absence of an external electric field, there is no need in the operator \mathcal{R}_{μ} .) As is easy to check, the Dirac gap $m_D \tilde{\Psi} \Psi$ breaks the U(2) symmetry down to $U_{+}(1) \times U_{-}(1)$, where $\tilde{\Psi} = \Psi^{\dagger} \tilde{\gamma}^0$ and the subscript $\lambda = \pm$ labels the two irreducible representations or the surfaces of the TI slab. The Haldane gap $m_H \tilde{\Psi} \tilde{\gamma}^3 \tilde{\gamma}^5 \Psi$ is invariant with respect to the U(2) symmetry, but, unlike the Dirac gap, it breaks the parity P and T symmetries. Since external electric and magnetic fields break P and T symmetries, the generation of the Haldane gap has no effect on symmetry breaking. Therefore, only the dynamically generated Dirac gap will spontaneously break the symmetry

of our model. As we will see below, such a gap is indeed generated due to the electrified magnetic catalysis.

For numerical calculations, it is useful to estimate energy scales in the problem at hand:

$$\Delta_{\text{bulk}} \approx 350 \text{ meV}, \quad \frac{g_s \mu_B B}{2} \approx 0.5 B [T] \text{ meV},$$

$$\epsilon_B = \sqrt{2v_F^2 |eB|} \approx 22.6 \sqrt{B [T]} \text{ meV},$$

$$l \approx 25.7 \text{ nm} / \sqrt{B [T]}. \quad (30)$$

By solving numerically the gap equations (22), (23), and (24) together with constraint (25), we straightforwardly obtain the electrochemical potentials $\mu_{n,\pm}$ and the gaps $m_{n,\pm}$ as functions of the magnetic field. The results for the lowest and first Landau level parameters are shown in Fig. 1 for fixed values of the electric field and temperature $\mathcal{E} = 1 \text{ mV/\AA}$ and $T = 5 \times 10^{-3} \Delta_{\text{bulk}} \approx 20 \text{ K}$, respectively. In the calculation, we truncated the system of equations by including only $n_{\text{max}} = 26$ Landau levels.

As we see from the left panel in Fig. 1, the absolute values of the electrochemical potentials $\Delta_{\text{eff},\pm}$ and $\mu_{1,\pm}$ experience a large jump around $|B| \approx 5 \text{ T}$. The jump corresponds to the point at which the filling of the first Landau level starts. We checked that the position of the jump shifts to larger values of the magnetic field with increasing the external electric field. Of course, this behavior is expected since larger electric fields require higher charge densities on the TI surfaces. In addition to the large jump around $|B| \approx 5 \text{ T}$, we also observe additional features in the dependence of $\Delta_{\text{eff},\pm}$ and $\mu_{1,\pm}$ at smaller values of the magnetic field. They generically correspond to the onset of filling of higher Landau levels. Here, it is appropriate to mention that, in all regimes studied, the electrochemical potentials $\mu_{\pm}^{(0)}$ are very similar quantitatively to $\mu_{1,\pm}$ and, therefore, we do not show them in our figures.

Let us now turn to the discussion of the dynamically generated gaps. The results in the middle panel of Fig. 1 clearly demonstrate that the surface gaps $m_{1,\pm}$ monotonically increase with the magnetic field. More interestingly, however, we find that the values of the gaps on the two surfaces $m_{1,+}$ and $m_{1,-}$ remain comparable, although not identical to each other for sufficiently weak electric fields. The importance of this observation becomes obvious in the context of the U(2) symmetry discussed earlier. Indeed, if the values of $m_{1,+}$ and $m_{1,-}$ were exactly the same, they would describe a pure Haldane solution. As is clear from the definition in Eq. (26), a small difference between $m_{1,+}$ and $m_{1,-}$ implies the existence

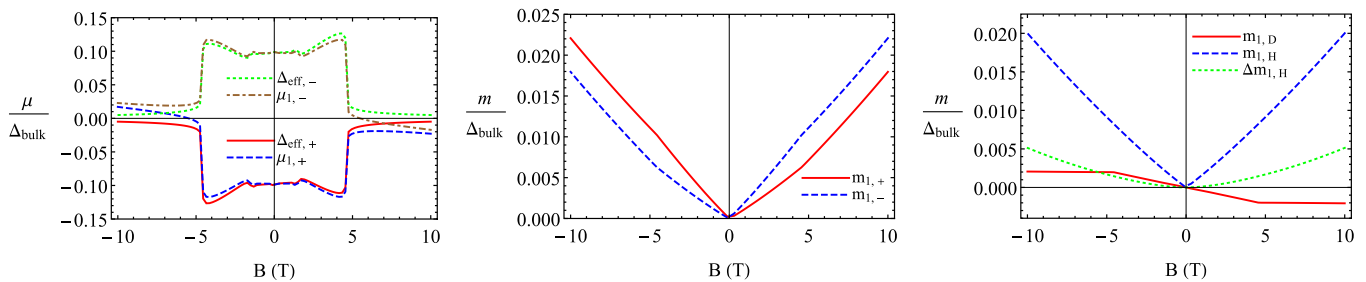


FIG. 1. The lowest and first Landau level parameters as functions of the magnetic field for fixed values of the external electric field $\mathcal{E} = 1 \text{ mV/\AA}$ and temperature $T = 5 \times 10^{-3} \Delta_{\text{bulk}} \approx 20 \text{ K}$. The results for the (effective) electrochemical potentials $\Delta_{\text{eff},\pm}$ and $\mu_{1,\pm}$ are shown in the left panel, the gaps $m_{1,\pm}$ are shown in the middle panel, and Dirac and Haldane gaps $m_{1,D}$, $m_{1,H}$, and $\Delta m_{1,H}$ are shown in the right panel.

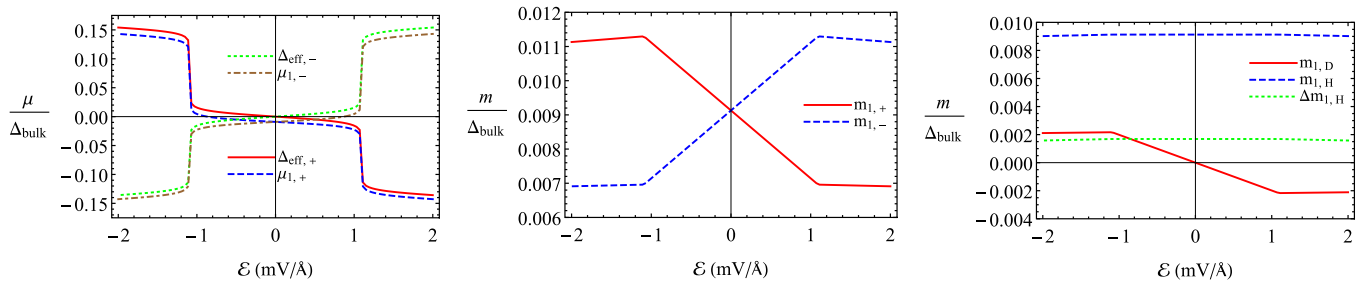


FIG. 2. The lowest and first Landau level parameters as functions of the external electric field for fixed values of the magnetic field $B = 5$ T and temperature $T = 5 \times 10^{-3} \Delta_{\text{bulk}} \approx 20$ K. The results for the (effective) electrochemical potentials $\Delta_{\text{eff},\pm}$ and $\mu_{1,\pm}$ are shown in the left panel, the gaps $m_{1,\pm}$ are shown in the middle panel, and Dirac and Haldane gaps $m_{1,D}$, $m_{1,H}$, and $\Delta m_{1,H}$ are shown in the right panel.

of a dynamically generated Dirac gap. Such a gap is induced by the applied electric field. This conclusion is further supported by the dependence of the dynamical gaps on the electric field, shown in Fig. 2 and discussed below Eq. (33).

The results in the right panel of Fig. 1 demonstrate that the absolute value of the Dirac gap $m_{1,D}$ increases with the magnetic field at sufficiently small fields $|B| \lesssim 5$ T, when the LLL is fully filled. At larger magnetic fields $|B| \gtrsim 5$ T, when the LLL is not fully filled, the Dirac gap remains nearly constant (or increases very slowly). In contrast, the dynamical part of the Haldane gap $\Delta m_{1,H}$ increases approximately as B^2 . Note that, because of the linear dependence of $m^{(0)}$ on the magnetic field, the total Haldane gap $m_{1,H}$ grows almost linearly with B .

The dependencies of the lowest and first Landau level parameters on the external electric field are presented in Fig. 2 for fixed values of the magnetic field ($B = 5$ T) and temperature ($T = 5 \times 10^{-3} \Delta_{\text{bulk}} \approx 20$ K). As we see from the left panel in Fig. 2, the absolute values of the electrochemical potentials slowly increase with electric field at first, and then experience a substantial jump at $|\mathcal{E}| \approx 1$ mV/Å. The jump corresponds to the field at which the filling of the first Landau level begins. From the middle panel in Fig. 2, we see that the surface gaps $m_{1,\pm}$ have a linear dependence at weak fields (i.e., in the regime of a partially filled LLL) and stay approximately constant at higher electric fields. As might have been expected, the Haldane gap $m_{1,H}$, which is shown in the right panel of Fig. 2, depends very weakly on the applied electric field. This is in contrast to the behavior of the Dirac gap $m_{1,D}$ (see the right panel in Fig. 2), which is linear in \mathcal{E} at small fields and stays approximately constant at large fields. It should be also emphasized that the Dirac gap vanishes at $\mathcal{E} = 0$. As we argue below, this fact is important from the viewpoint of symmetry properties in the model.

As already suggested earlier, the generation of the Dirac gap is directly connected with the applied external electric field. In order to demonstrate this in the simplest possible setting, it is instructive to consider an approximate form of the gap equation (23) in the limit of a large magnetic field. By rewriting it in terms of the Haldane and Dirac gaps, we obtain

$$m_{n,H} \approx m^{(0)} + \frac{1}{4l} \sum_{n'=1}^{\infty} \times \left(\alpha v_F \mathcal{K}_{n'-1,n-1}^{(0)} + \alpha v_F \mathcal{K}_{n',n}^{(0)} + \frac{G_{\text{int}}}{\pi l} \right) \frac{m_{n',H}}{M_{n'}}, \quad (31)$$

$$m_{n,D} \approx -\pi l s_B \epsilon_0 \left(\alpha v_F \mathcal{K}_{0,n}^{(0)} + \frac{G_{\text{int}}}{2\pi l} \right) \frac{\mathcal{E}}{e} + \frac{1}{4l} \sum_{n'=1}^{\infty} \times \left(\alpha v_F \mathcal{K}_{n'-1,n-1}^{(0)} + \alpha v_F \mathcal{K}_{n',n}^{(0)} + \frac{G_{\text{int}}}{\pi l} \right) \frac{m_{n',D}}{M_{n'}}, \quad (32)$$

where we took into account that $n_F(M_n \pm \mu_{n,\lambda}) \ll 1$ for $n \geq 1$ and assumed that $M_{n'}$ is almost independent of the small Dirac gap. Note that in order to rewrite the LLL contributions in the gap equations in terms of the electric field \mathcal{E} , we used the following approximate expression for the surface charge densities:

$$\rho_+ = -\rho_- = \frac{\rho_+ - \rho_-}{2} \approx \frac{e}{4\pi l^2} [n_F(\Delta_{\text{eff},+}) - n_F(\Delta_{\text{eff},-})] = \epsilon_0 \mathcal{E}. \quad (33)$$

By comparing the gap equations (31) and (32), we see that the external electric field plays the role of a “seed” for the Dirac gap $m_{n,D}$, just as the bare gap parameter $m^{(0)}$ for the Haldane gap $m_{n,H}$. This explains why the external electric field is the key factor in generating the Dirac gap and breaking the $U(2)$ symmetry in the slab of 3D TIs.

It may be instructive to study the dependence of the electrochemical potentials $\mu_{n,\pm}$ and gaps $m_{n,\pm}$ on the Landau level index n . The corresponding results for two different values of the electric field are presented in Fig. 3 for $B = 5$ T and $T = 5 \times 10^{-3} \Delta_{\text{bulk}} \approx 20$ K. As we see, all dynamical parameters depend very weakly on the Landau level index n . In view of the large surface dielectric constant and, consequently, weak Coulomb interaction, this result is not surprising. Moreover, it strongly suggests that the long-range interaction indeed plays a minor role compared to the local interaction.

By using the above results, we can also obtain the quasiparticle energy levels as functions of the magnetic and electric fields

$$\omega_{0,\lambda} = -\Delta_{\text{eff},\lambda}, \quad \omega_{n>0,\lambda} = -\mu_{n,\lambda} \pm M_n, \quad (34)$$

where M_n were given below Eq. (18). The corresponding numerical results are summarized in Fig. 4.

As we see from the left panel in Fig. 4, there is a rather large splitting between the energy levels on the top and bottom surfaces at small values of the magnetic field. This corresponds

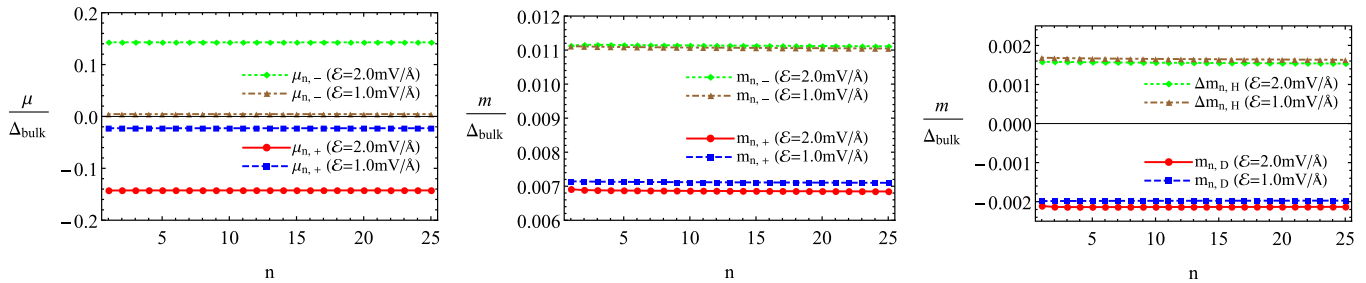


FIG. 3. The electrochemical potentials $\mu_{n,\pm}$ (left panel), the gaps $m_{n,\pm}$ (middle panel), and the Dirac and Haldane gaps (right panel) as functions of the Landau level index n . The results for $\mathcal{E} = 2 \text{ mV}/\text{\AA}$ are represented by red solid and green dotted lines. The results for $\mathcal{E} = 1 \text{ mV}/\text{\AA}$ are represented by blue dashed and brown dashed-dotted lines. The values of the magnetic field and temperature are $B = 5 \text{ T}$ and $T = 5 \times 10^{-3} \Delta_{\text{bulk}} \approx 20 \text{ K}$, respectively.

to the regime with higher Landau levels being occupied. With increasing the magnetic field, the magnitude of splitting quickly diminishes and becomes rather small when the LLL regime is reached. In contrast, the increase of the electric field tends to amplify the splitting between the Landau levels. The existence of such a splitting may lead to an observation of new plateaus in the Hall conductivity. The large jumps in the energy spectrum at $|B| \approx 5 \text{ T}$ and $|\mathcal{E}| \approx 1 \text{ mV}/\text{\AA}$ correspond to the onset of and the exit from the LLL regime, respectively. As is clear, these features are directly connected with the corresponding jumps in the electrochemical potentials, seen in the left panels of Figs. 1 and 2.

Before concluding this section, let us briefly discuss the role of finite temperature in our solution. As expected, the main results remain qualitatively the same for a whole range of sufficiently small values of the temperature. With increasing (decreasing) the temperature, however, the jumps that correspond to the onset of and the exit from the LLL regime become smoother (sharper) in the dependence of the electrochemical potentials on the fields, shown in the left panels of Figs. 1 and 2. It is also worth pointing that a weak dependence of electrochemical potentials on the fields in the regions between the jumps is caused by thermal broadening of Landau levels. It vanishes in the limit $T \rightarrow 0$.

V. INHOMOGENEOUS PHASE WITH TWO STRIPES: QUALITATIVE APPROACH

In the previous section, we advocated the homogeneous phase with dynamically generated gaps as the ground state of 3D TIs in a sufficiently strong external electric field. On the other hand, the inhomogeneous CDW phase considered in Ref. [19] is likely to be more favorable in weak electric fields. In order to provide a qualitative analytic description of the inhomogeneous CDW phase with a “stripe” pattern, in this section we consider a simple configuration of two stripes with an infinitely thin transition region, or a domain wall at $x = 0$. This is modeled by an inhomogeneous gap $m(x) = |m| \text{sign}(x)$ for the top surface, i.e., $\lambda = +1$ and $s_B = +1$. (Note that such a gap function with asymptotes of opposite sign at $x \rightarrow \pm\infty$, but without a magnetic field, is qualitatively similar to the famous Jackiw-Rebbi solution in 1D [47].)

The solution to the Dirac equation with the gap function in the form $m(x) = |m| \text{sign}(x)$ is discussed in Appendix A 3. The corresponding numerical results for the quasiparticle energy spectrum as a function of k_y , as well as the chiral condensate and charge density as functions of the spatial coordinate x , are shown in Fig. 5. In order to plot the results, we fixed the model parameters as follows: $m = 5 \text{ meV}$, $\mu = 0$, and $B = 5 \text{ T}$. In the calculation, we also limited the sum over

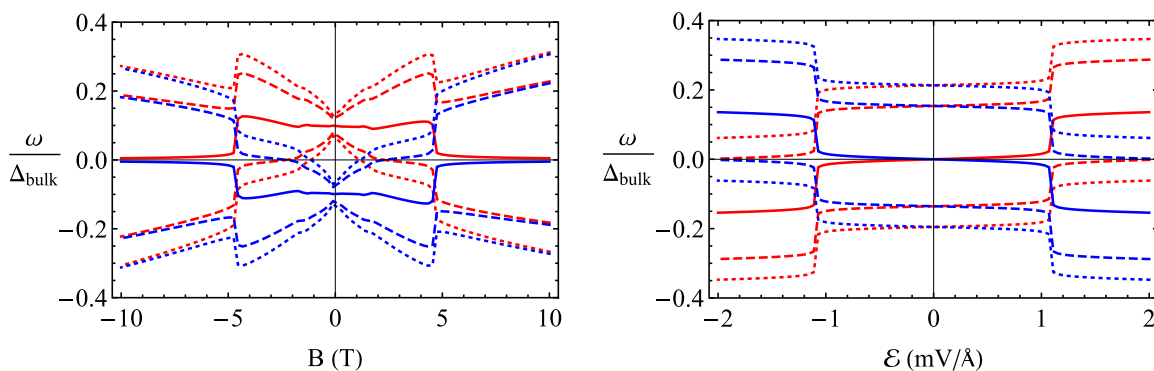


FIG. 4. The quasiparticle energies for the first three Landau levels as functions of the magnetic field at fixed $\mathcal{E} = 1 \text{ mV}/\text{\AA}$ (left panel) and as functions of the electric field at fixed $B = 5 \text{ T}$ (right panel). Red and blue lines denote the quasiparticle energies on the top and bottom surfaces, respectively. Solid lines represent the LLL, dashed and dotted lines correspond to the first and second Landau levels, respectively. The temperature is $T = 5 \times 10^{-3} \Delta_{\text{bulk}} \approx 20 \text{ K}$.

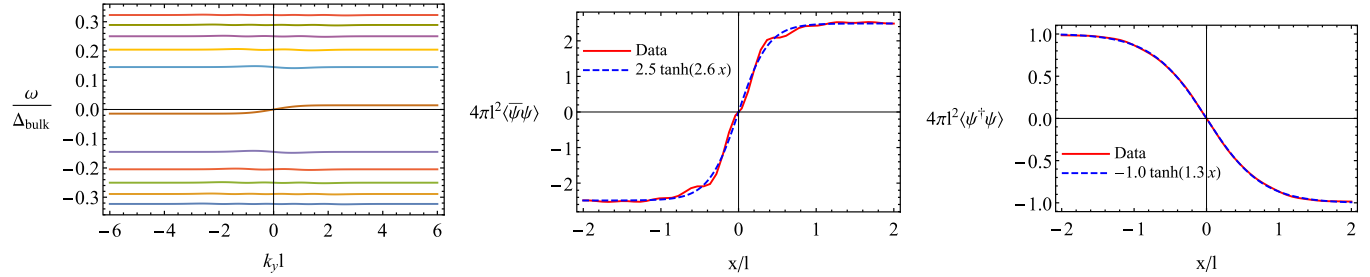


FIG. 5. The energy spectrum as a function of k_y (left panel), the chiral condensate (middle panel), and the charge density (right panel) as functions of x in the Dirac problem with the inhomogeneous gap $m(x) = |m| \text{sign}(x)$. For simplicity, only the first six Landau levels are presented in the left panel. The red solid lines in the middle and right panels represent the numerical data. The blue dashed lines denote the corresponding fits. The model parameters are $m = 5$ meV, $\mu = 0$, and $B = 5$ T.

Landau levels ($n_{\text{max}} = 26$) and cut off the integration over k_y ($-6/l \leq k_y \leq 6/l$).

As we see from Fig. 5, the chiral condensate and the charge density have a kink and antikink structure, respectively. Therefore, the existence of zero-energy states on the domain wall agrees with the inhomogeneous form of the gap function. The chiral condensate and the charge density can be fitted well by the following functions:

$$\begin{aligned} \text{tr}[G(u,u)] &= \sum_n \frac{\text{sign}(\omega_n)}{2} \bar{\psi}_{\omega_n}(x) \psi_{\omega_n}(x) \\ &\approx \frac{1}{4\pi l^2} 2.5 \tanh\left(2.6 \frac{x}{l}\right), \end{aligned} \quad (35)$$

$$\begin{aligned} \text{tr}[\gamma^0 G(u,u)] &= \sum_n \frac{\text{sign}(\omega_n)}{2} \psi_{\omega_n}^\dagger(x) \psi_{\omega_n}(x) \\ &\approx -\frac{1}{4\pi l^2} 1.0 \tanh\left(1.3 \frac{x}{l}\right), \end{aligned} \quad (36)$$

where the sum runs over the complete set of eigenstates, given by the solutions to the spectral equation (A18). These fits are shown in Fig. 5 alongside with the numerical solutions.

Let us now consider the case of a nonzero external electric field, applied perpendicularly to the slab. By considering a sufficiently thick slab, we will assume that the average electric field inside the slab vanishes. In the homogeneous case, the field is screened by the uniform surface charge densities. This generically requires specific nonzero electrochemical potentials μ_{\pm} on the top and bottom TIs surfaces. In the inhomogeneous striped phase, however, the simplest way to achieve nonzero average surface charge densities is to vary the width of stripes by Δl_x . The value of Δl_x can be estimated from the following expression:

$$\begin{aligned} \epsilon_0 \mathcal{E} &= \rho(l_x + \Delta l_x) - \rho(l_x) + \rho(-l_x + \Delta l_x) - \rho(-l_x) \\ &\approx \frac{e}{4\pi l^2} \left[\tanh\left(1.3 \frac{l_x + \Delta l_x}{l}\right) - \tanh\left(1.3 \frac{l_x - \Delta l_x}{l}\right) \right], \end{aligned} \quad (37)$$

where we used the standard definition for the surface charge density $\rho = e \text{tr}[\gamma^0 G(u,u)]$ together with Eq. (36).

Our numerical result for the ratio of the correction Δl_x to the stripe half-width l_x is plotted in Fig. 6. We see that the correction to the stripe width Δl_x becomes significant at

sufficiently strong electric fields. In fact, it is comparable to l_x already for $\mathcal{E} \gtrsim 1$ mV/Å. This suggests that the stripe phase is unstable when the electric field exceeds a certain critical value \mathcal{E}_{cr} . Quantitatively, the critical value roughly corresponds to the beginning of the first Landau level filling

$$\mathcal{E}_{\text{cr}} \approx \frac{e^2 B}{4\pi \epsilon_0 \hbar c}, \quad (38)$$

where we used Eq. (25) and restored Planck's constant \hbar and the speed of light c . This relation implies that $\mathcal{E}_{\text{cr}} \approx 0.22 B[\text{T}]$ mV/Å, which is in a good agreement with our previous numerical estimate $\mathcal{E} \gtrsim 1$ mV/Å at $B = 5$ T.

Another way to estimate the critical value of the electric field is to compare the free-energy density in the homogeneous phase, which is given by Eq. (B12), with the energy density of the stripe phase estimated in Ref. [19]. In other words, the value of \mathcal{E}_{cr} is given by the solution to the following equation:

$$0 = \sum_{\lambda} \Omega_{\lambda} - \left[\frac{\sqrt{\alpha \gamma}}{l^2} - \frac{m}{l^2} \right], \quad (39)$$

where the term in square brackets corresponds to the energy cost of creating the stripe phase [19]. The latter is characterized by the domain-wall tension $\gamma \sim 1/l^2$ and the magnetic mass $m \sim 1/l$. The value of α is given below Eq. (19). The solution to Eq. (39) can be easily obtained numerically and appears to

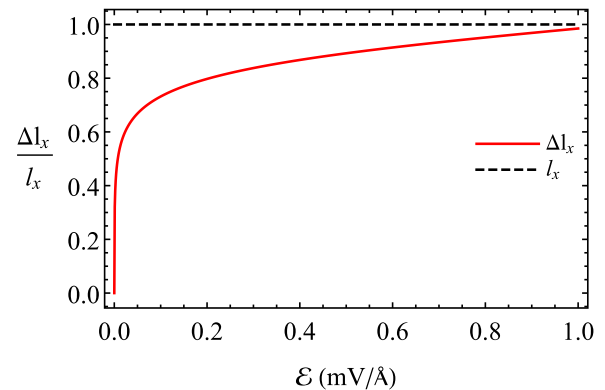


FIG. 6. The ratio of the width correction Δl_x to the stripe half-width l_x as a function of the external electric field (red line). The model parameters are $m = 5$ meV, $\mu = 0$, $B = 5$ T, and $l_x = 500$ Å.

agree quite well with the estimate in Eq. (38). One can also obtain an approximate analytical solution to Eq. (39) by using the LLL approximation for the free-energy density (B12), i.e.,

$$\Omega_\lambda \approx \frac{\lambda \epsilon_0 \mathcal{E} \Delta_{\text{eff}}}{e}, \quad (40)$$

where we used the LLL approximation for the charge density (25). Then, by substituting this into Eq. (39) and estimating the effective electrochemical potential as $\Delta_{\text{eff}} \sim \lambda/l$, we find the following critical value of the electric field:

$$\mathcal{E}_{\text{cr}} \approx \frac{e^2 B(1 - \sqrt{\alpha})}{2\epsilon_0 \hbar c}. \quad (41)$$

This result is qualitatively the same as the estimate in Eq. (38), although quantitatively appears to be somewhat larger, $\mathcal{E}_{\text{cr}} \approx 1.03 B[\text{T}] \text{ mV}/\text{\AA}$. We conclude, therefore, that the critical electric field scales linearly with the magnetic field $\mathcal{E}_{\text{cr}} \sim e^2 B/(\epsilon_0 \hbar c)$, but the coefficient of proportionality is determined only up to an overall factor of order 1.

VI. DISCUSSION

In this section, we discuss the range of validity and limitations of our study, and compare our main results with those existing in the literature. Let us start by pointing the limitation of our model used for the description of the TI surface states. While the model captures the Dirac nature of the low-energy quasiparticles, it does not describe the hexagonal warping of the Fermi surface that occurs away from the Dirac point [7,11]. The corresponding effect was taken into account in the study of gap generation in Ref. [48] and could play an essential role in some TIs. For example, this may be the case in Bi_2Te_3 [e.g., see Fig. 1(c) in Ref. [11]], in which the band gap is about three times smaller than in Bi_2Se_3 and the trigonal potential $\sim k^3$ is rather strong. In the case of Bi_2Se_3 , however, the hexagonal warping could be safely neglected, except for the case of rather high values of the chemical potential [e.g., see Fig. 8 in Ref. [4] and Fig. 3(b) in Ref. [12]]. The model used in this study also ignores a Schrödinger-type term $\sim k^2$, which describes an asymmetry between the electron and hole bands [49] (see also Fig. 1 in Ref. [12]). When the quadratic term is sufficiently small, it is not expected to substantially affect the dynamics of the gap generation.

The study here did not include the effects of the intersurface tunneling on the dynamical generation of gaps. According to Ref. [26], tunneling between the opposite surfaces may be quite important only for sufficiently thin ($l_z \lesssim 8 \text{ nm}$) TI slabs. Therefore, neglecting the intersurface tunneling is expected to be a good approximation in the case of thick samples. It would be interesting, however, to rigorously study the corresponding effects in thin TI films in external electric and magnetic fields.

One of the uncertainties of the model Hamiltonian used in this study is the strength of the local interaction G_{int} . Although the order of magnitude of this coupling constant could be estimated by using general arguments, its precise value is unknown. Despite this, we argue that the simplified model (4) that includes both short- and long-range interactions (6) is sufficient for the qualitative analysis of the electrified magnetic catalysis in 3D TIs. Moreover, we might even suggest that,

irrespective of the specific value of the coupling constants, the qualitative features established here should be rather universal.

It is interesting to compare our results with those obtained in Ref. [19], where the phase diagram was studied in 3D TIs in a magnetic field, but without an external electric field. The authors of Ref. [19] argued that, depending on the strength of local interaction, the CFL or CDW (“stripe” or “bubble”) phases can be realized. Our results here suggest that neither of those two phases describe the ground state of the TI slab in a sufficiently strong external electric field. The CFL phase with the half-filled LLL on each TI surface cannot be easily deformed to screen out the external electric field from penetrating into the TI bulk. This would imply a large energy cost and disfavor the CFL phase. The CDW phase could perhaps survive when a relatively weak electric field is applied. In this case, the average charge densities on the TI surfaces, which are needed to screen the electric field out from the bulk, could be simply obtained by the formation of positive and negative stripes (or bubbles) of unequal size. (Note that it is energetically favorable to have either completely filled or empty LLL inside the stripes [19].) As we showed in Sec. V, a simple estimate suggests that the charge imbalance obtained by the variation of the stripe widths can compensate only relatively weak electric fields. Therefore, a sufficiently strong electric field $\mathcal{E} > \mathcal{E}_{\text{cr}}$ also destroys the CDW phase. Our parametric estimate for the critical electric field strength is $\mathcal{E}_{\text{cr}} \sim e^2 B/(\epsilon_0 \hbar c)$.

In view of the above arguments, we claim that the ground state of the TI slab in a nonzero magnetic field and a sufficiently strong electric field is a homogeneous phase with equal in magnitude, but opposite in sign, surface charge densities. It is also characterized by the presence of both Dirac and Haldane gaps. While our qualitative conclusion seems rather rigorous, this study is insufficient to establish the precise structure of the phase diagram in the plane of the applied electric and magnetic fields. It would be very interesting to clarify the details of the corresponding phase diagram either experimentally or numerically.

It may be instructive to note that the thermal broadening of Landau levels plays a relatively important technical role in our analysis and in the description of the electrified homogeneous phases. Indeed, by using a nonzero temperature, we were able to unambiguously describe the surface ground states with adjustable partial fillings of Landau levels, needed to screen the external electric field. Certainly, the corresponding ground states allow a well-defined zero-temperature limit, but their description may become more subtle. By noting that surface impurities also broaden Landau levels, we suggest that their presence could lead to a realization of the electrified magnetic catalysis similar to that in Sec. IV.

As is clear from our study, the low-energy model for the surface states of 3D TIs is essentially a (2+1)-dimensional QED, supplemented by certain constraints. The generation of different types of gaps, such as those describing spontaneous parity breaking and chiral symmetry breaking were studied in QED_{2+1} without background electromagnetic fields in Refs. [33,35,50] a long time ago. Moreover, it was shown that the Dirac mass can be spontaneously generated, while the Haldane mass is energetically disfavored [35]. Clearly, this

is not the case in the problem at hand, where both types of gaps are generated on the TI surfaces. This is due to the fact that the TR and inversion symmetries are explicitly broken by the external magnetic and electric fields. Furthermore, we find that the Haldane gap dominates at small values of the electric field. This situation is reminiscent of the dynamically enhanced Zeeman splitting in graphene [39].

VII. CONCLUSION

In this study, we considered the dynamical generation of gaps in a slab of a 3D TI, such as Bi₂Se₃, placed in the magnetic and electric fields perpendicular to its surfaces. (Although we used the model parameters for Bi₂Se₃, the main conclusions should be valid for all similar TIs.) Note that the conducting states on the TI slab surfaces and the overall geometry of the system are rather similar to bilayer graphene. On the other hand, the degeneracy connected with the valley and spin degrees of freedom, which is responsible for a variety of quantum Hall states in bilayer graphene, is absent in a TI slab. Still, there are notable similarities in the dynamics of gap generation in these two physical systems. For example, the valley quantum Hall (or layer polarized) state, which is realized in a sufficiently strong external electric field in bilayer graphene, resembles the homogeneous state considered in this paper.

By solving the gap equations for the surface quasiparticle propagators in a simple model with short- and long-range interactions, we found that *both* the Dirac and Haldane gaps are dynamically generated in the TI slab in external electric and magnetic fields. The underlying mechanism is a different version of the magnetic catalysis. Because of a large surface dielectric constant, the Coulomb interaction appears to play a minor role in the dynamics. Unlike the Dirac gap, the Haldane gap respects the U(2) symmetry with the generators given in Eq. (29), but breaks the parity and TR symmetries. Since both discrete symmetries are explicitly broken by external electric and magnetic fields, the generation of the Haldane gap does not break any symmetries. The Dirac gap, on the other hand, is generated only in the presence of an electric field. The result of such an *electrified* magnetic catalysis is a spontaneous breaking of the U(2) symmetry.

By comparing our results with the findings in Ref. [19], we argued that the homogeneous phase with dynamically generated Dirac and Haldane gaps is the true ground state in the TI slab in nonzero magnetic and sufficiently strong electric fields. The precise structure of the phase diagram in the plane of applied electric and magnetic fields remains to be clarified, however.

ACKNOWLEDGMENTS

The authors are grateful to V. P. Gusynin for useful discussions. The work of E.V.G. was supported partially by the Ukrainian State Foundation for Fundamental Research. The work of V.A.M. and P.O.S. was supported by the Natural Sciences and Engineering Research Council of Canada. The work of I.A.S. was supported in part by the U. S. National Science Foundation under Grant No. PHY-1404232.

APPENDIX A: WAVE FUNCTIONS AND FERMION PROPAGATOR

In this appendix, we determine the wave functions and the fermion propagator in the model with the free Hamiltonian in Eq. (2). For the simplicity of notation, we will drop the superscript (0) in $\mu_\lambda^{(0)}$ and $m_\lambda^{(0)}$ in this appendix.

1. Wave functions

The eigenvalue problem $H_\lambda^{(0)}\psi = \omega\psi$ for the model Hamiltonian in Eq. (2) reduces to the following equation:

$$\begin{pmatrix} m_\lambda - \mu_\lambda & v_F(\partial_x + s_B k_y + eBx) \\ v_F(-\partial_x + s_B k_y + eBx) & -m_\lambda - \mu_\lambda \end{pmatrix} \times \phi(x) = \omega\phi(x), \quad (\text{A1})$$

after we choose the wave function in the form $\psi(\mathbf{r}) = e^{is_B k_y y} \phi(x)$, where $\phi(x) = (\phi_1(x), \phi_2(x))^T$ and $s_B = \text{sign}(eB)$. It terms of the variable

$$\xi = \sqrt{|eB|} \left(\frac{k_y}{|eB|} + x \right), \quad (\text{A2})$$

Eq. (A1) can be rewritten in the form

$$(m_\lambda - \mu_\lambda - \omega)\phi_1(\xi) + v_F\sqrt{|eB|}(\partial_\xi + s_B\xi) \times \phi_2(\xi) = 0, \quad (\text{A3})$$

$$v_F\sqrt{|eB|}(-\partial_\xi + s_B\xi)\phi_1(\xi) - (m_\lambda + \mu_\lambda + \omega)\phi_2(\xi) = 0. \quad (\text{A4})$$

For simplicity, here we consider only the case with $s_B = +1$. The solutions to this system of equations take the form

$$\phi_1(\xi) = \frac{v_F\sqrt{2|eB|}}{\mu_\lambda + \omega - m_\lambda} \frac{p^2}{2} D_{p^2/2-1}(\sqrt{2}\xi), \quad (\text{A5})$$

$$\phi_2(\xi) = D_{p^2/2}(\sqrt{2}\xi), \quad (\text{A6})$$

where $p = \sqrt{(\omega + \mu_\lambda)^2 - m_\lambda^2}/(v_F\sqrt{|eB|})$ and $D_{p^2/2}(\sqrt{2}\xi)$ is the parabolic cylinder function [51]. By requiring that solutions are finite at $|\xi| \rightarrow \infty$, we find the quantization condition $p^2/2 = n$, where n is a non-negative integer. In this special case, the parabolic cylinder functions can be expressed in terms of Hermitian polynomials $H_n(\xi)$, i.e.,

$$D_n(\sqrt{2}\xi) = \frac{e^{-\xi^2/2} H_n(\xi)}{\sqrt{2^n}}. \quad (\text{A7})$$

Thus, the final expressions for the normalized wave functions take the form

$$\psi_{s_B=+1,n}(\mathbf{r}) = \frac{1}{\sqrt{2l}} \sqrt{\frac{\omega_n + \mu_\lambda - m_\lambda}{\omega_n + \mu_\lambda}} e^{ik_y y} \begin{pmatrix} \frac{v_F\sqrt{2n|eB|}}{\mu_\lambda + \omega_n - m_\lambda} Y_{n-1}(\xi) \\ Y_n(\xi) \end{pmatrix}, \quad (\text{A8})$$

where $Y_n(\xi) = \frac{e^{-\xi^2/2} H_n(\xi)}{\sqrt{2^n n! \sqrt{\pi}}}$ and $l = 1/\sqrt{|eB|}$ is the magnetic length. Note that the normalized wave function in the case of $s_B = -1$ is given by $\psi_{s_B=-1,n}(\mathbf{r}) =$

$(-i\sigma_y)\psi_{s_B=+1,n}^*(\mathbf{r})|_{m_\lambda \rightarrow -m_\lambda}$. The corresponding energy eigenvalues are

$$\omega_{n=0} = -\mu_\lambda - s_B m_\lambda, \quad \omega_{n>0} = -\mu_\lambda \pm M_n, \quad (\text{A9})$$

where $M_n = \sqrt{m_\lambda^2 + n\epsilon_B^2}$ and $\epsilon_B = \sqrt{2v_F^2|eB|}$ is the Landau energy scale.

2. Fermion propagator

In this section we derive the free fermion propagator in the model under consideration. In the mixed frequency-coordinate

space representation, the fermion (Feynman) propagator is formally defined by

$$S(\omega, \mathbf{r}, \mathbf{r}') \equiv i \sum_n \frac{\psi_n(\mathbf{r})\bar{\psi}_n(\mathbf{r}')}{\omega - \omega_n + i0 \text{sign}(\omega)}, \quad (\text{A10})$$

where the sum runs over the complete set of quasiparticle eigenstates given by Eq. (A9).

It is convenient to start with the derivation of the lowest Landau level (LLL) contribution to the fermion propagator, i.e.,

$$S_{n=0}(\omega, \mathbf{r}, \mathbf{r}') = i \int \frac{dk_y}{2\pi} \frac{\psi_{n=0}(\mathbf{r})\bar{\psi}_{n=0}(\mathbf{r}')}{\omega + \mu_\lambda + s_B m_\lambda + i0 \text{sign}(\omega)} = -i s_B \frac{P_-}{2\pi l^2} \frac{e^{i\Phi(\mathbf{r}, \mathbf{r}') - \eta/2}}{\omega + \mu_\lambda + s_B m_\lambda + i0 \text{sign}(\omega)}, \quad (\text{A11})$$

where $P_\pm = (1 \pm s_B \gamma^0)/2$, $\Phi(\mathbf{r}, \mathbf{r}') = -eB(x + x')(y - y')/2$ is the Schwinger phase, and $\eta = (\mathbf{r} - \mathbf{r}')^2/(2l^2)$.

The contribution of higher Landau levels to the fermion propagator is given by

$$S_{n>0}(\omega, \mathbf{r}, \mathbf{r}') = \sum_{n=1}^{\infty} \frac{i e^{i\Phi(\mathbf{r}, \mathbf{r}') - \eta/2}}{2\pi l^2} \left\{ \frac{s_B(\omega + \mu_\lambda)[L_{n-1}(\eta)P_+ - L_n(\eta)P_-]}{[\omega + \mu_\lambda + i0 \text{sign}(\omega)]^2 - M_n^2} + \frac{m_\lambda[L_{n-1}(\eta)P_+ + L_n(\eta)P_-] - i \frac{v_F}{l^2} L_{n-1}^1(\eta)[\boldsymbol{\gamma} \cdot (\mathbf{r} - \mathbf{r}')] }{[\omega + \mu_\lambda + i0 \text{sign}(\omega)]^2 - M_n^2} \right\}, \quad (\text{A12})$$

where $L_n^j(x)$ are the generalized Laguerre polynomials (by definition $L_n \equiv L_n^0$). In the derivation, we performed the summation over the quasiparticle energies and integrated over k_y by using formula 7.377 in Ref. [52].

In the case of a nonzero temperature, the energies are replaced by the Matsubara frequencies, i.e., $\omega \rightarrow i\omega_{m'} = i\pi T(2m' + 1)$. In the gap equation (19), the corresponding propagators enter in the form of a sum over Matsubara frequencies. The corresponding results for the sums are

$$T \sum_{m'=-\infty}^{\infty} S_{n=0}(i\omega_{m'}, \mathbf{r}, \mathbf{r}') = \frac{s_B P_- e^{i\Phi(\mathbf{r}, \mathbf{r}') - \eta/2}}{2\pi l^2} \frac{1 - 2n_F(\mu_\lambda + s_B m_\lambda)}{2}, \quad (\text{A13})$$

$$T \sum_{m'=-\infty}^{\infty} S_{n>0}(i\omega_{m'}, \mathbf{r}, \mathbf{r}') = -\frac{e^{i\Phi(\mathbf{r}, \mathbf{r}') - \eta/2}}{4\pi l^2} \sum_{n=1}^{\infty} \left\{ [n_F(M_n - \mu_\lambda) - n_F(M_n + \mu_\lambda)][L_{n-1}(\eta)P_+ - L_n(\eta)P_-] + \left[m_\lambda[L_{n-1}(\eta)P_+ + L_n(\eta)P_-] - i \frac{v_F}{l^2} L_{n-1}^1(\eta)[\boldsymbol{\gamma} \cdot (\mathbf{r} - \mathbf{r}')] \right] \frac{n_F(M_n + \mu_\lambda) + n_F(M_n - \mu_\lambda) - 1}{M_n} \right\}, \quad (\text{A14})$$

where $n_F(x) = 1/(e^{x/T} + 1)$ is the Fermi-Dirac distribution function.

3. Two stripes separated by a domain wall

In this section, we consider the Dirac problem with the inhomogeneous gap in the form $m(x) = |m| \text{sign}(x)$, which models an infinitely thin transition region at $x = 0$ that separates two wide stripes of phases with masses of opposite signs. For the sake of simplicity, we set $\lambda = +1$ and $s_B = +1$ in this section.

By making use of wave functions found in Appendix A 1, we obtain the following solutions in the regions with positive and negative gaps:

$$x > 0: \quad \phi_1(\xi) = \frac{v_F \sqrt{2|eB|}}{\mu + \omega - |m|} \frac{p^2}{2} D_{\frac{v^2}{2} - 1}(\sqrt{2}\xi), \quad \phi_2(\xi) = D_{\frac{v^2}{2}}(\sqrt{2}\xi), \quad (\text{A15})$$

$$x < 0: \quad \phi_1(\xi) = -\frac{v_F \sqrt{2|eB|}}{\mu + \omega + |m|} \frac{p^2}{2} D_{\frac{v^2}{2} - 1}(-\sqrt{2}\xi), \quad \phi_2(\xi) = D_{\frac{v^2}{2}}(-\sqrt{2}\xi), \quad (\text{A16})$$

where we assumed that the corresponding wave functions must vanish at $x \rightarrow \pm\infty$. By matching the wave functions at $x = 0$, i.e.,

$$C_+ \psi_{x>0} \Big|_{x=0} = C_- \psi_{x<0} \Big|_{x=0}, \quad (\text{A17})$$

we derive the following spectral equation:

$$\frac{D_{\frac{p^2}{2}-1}(\sqrt{2}k_y l)}{D_{\frac{p^2}{2}}(\sqrt{2}k_y l)} \frac{1}{\omega + \mu - |m|} = -\frac{D_{\frac{p^2}{2}-1}(-\sqrt{2}k_y l)}{D_{\frac{p^2}{2}}(-\sqrt{2}k_y l)} \frac{1}{\omega + \mu + |m|}. \quad (\text{A18})$$

Note that this spectral equation looks somewhat similar to Eq. (2.19) for bound states in Ref. [28]. We note, however, that the wave function in our case decreases at $|x| \rightarrow \infty$ polynomially rather than exponentially.

By making use of the wave functions, we can also give the following explicit results for the density of charge carriers (plus sign) and the chiral condensate (minus sign):

$$\begin{aligned} \text{tr}[(\gamma^0)^{\frac{1+\lambda}{2}} G(u, u)] &= \int \frac{dk_y}{2\pi} \sum_n \frac{\text{sign}[\omega_n(k_y)]}{2} |C_+[\omega_n(k_y) + \mu, k_y]|^2 \left\{ \theta(x) \left[\frac{[\omega_n(k_y) + \mu + |m|]^2}{\epsilon_B^2} \left| D_{v_n-1} \left(\sqrt{2}k_y l + \sqrt{2} \frac{x}{l} \right) \right|^2 \right. \right. \\ &\pm \left. \left| D_{v_n} \left(\sqrt{2}k_y l + \sqrt{2} \frac{x}{l} \right) \right|^2 \right] + \theta(-x) \left[\frac{D_{v_n}(\sqrt{2}k_y l)}{D_{v_n}(-\sqrt{2}k_y l)} \right]^2 \\ &\times \left. \left[\frac{[\omega_n(k_y) + \mu - |m|]^2}{\epsilon_B^2} \left| D_{v_n-1} \left(-\sqrt{2}k_y l - \sqrt{2} \frac{x}{l} \right) \right|^2 \pm \left| D_{v_n} \left(-\sqrt{2}k_y l - \sqrt{2} \frac{x}{l} \right) \right|^2 \right] \right\}, \quad (\text{A19}) \end{aligned}$$

where $\omega_n(k_y)$ denotes the roots of Eq. (A18), $v_n = [[\omega_n(k_y) + \mu]^2 - m^2]/\epsilon_B^2$, and $C_+(\omega, k_y)$ is a normalization constant. Note that contrary to the homogeneous phase, $\omega_n(k_y)$ now explicitly depends on k_y .

APPENDIX B: EFFECTIVE ACTION

In this appendix, we derive the one-loop Baym-Kadanoff (BK) effective action for the full surface quasiparticle propagators G_λ . We begin with the part of the effective action connected with the Coulomb interaction. (For a similar derivation in bilayer graphene, see Ref. [41].) The interaction Hamiltonian H_{int} of the Coulomb interaction in 3D has the standard form

$$H_{\text{int}} = \frac{e^2}{8\pi\epsilon_0\kappa} \int d^2\mathbf{r} dz d^2\mathbf{r}' dz' \frac{n(\mathbf{r}, z)n(\mathbf{r}', z')}{\sqrt{(\mathbf{r} - \mathbf{r}')^2 + (z - z')^2}}, \quad (\text{B1})$$

where $\epsilon_0 \approx 8.854 \times 10^{-12}$ F/m is the vacuum dielectric constant and κ is a dielectric permittivity. Since we wish to consider a TI slab in an external electric field, the density of charge carriers in the system under consideration consists of four terms:

$$n(\mathbf{r}, z) = \delta(z - L_z)n_{c,-} + \delta(z - l_z)n_-(\mathbf{r}) + \delta(z + l_z)n_+(\mathbf{r}) + \delta(z + L_z)n_{c,+}, \quad (\text{B2})$$

where $n_{c,\lambda}$ denote the densities of charge carriers on the capacitor plates separated by the distance $2L_z$ (clearly, we assume that these charge densities are uniform and do not depend on \mathbf{r} in order to produce constant electric field in which our TI slab is situated), and $n_\lambda(\mathbf{r}) = \psi_\lambda^\dagger(\mathbf{r})\psi_\lambda(\mathbf{r})$ denotes the density of charge carriers on the surfaces of the slab whose width is $2l_z$. Obviously, we assume that $L_z > l_z$.

By using Eq. (B2), we can easily integrate over z in Eq. (B1). The result reads as

$$\begin{aligned} H_{\text{int}} &= \frac{1}{2} \int d^2\mathbf{r} d^2\mathbf{r}' \{ U(\mathbf{r} - \mathbf{r}') [n_+(\mathbf{r})n_+(\mathbf{r}') + n_-(\mathbf{r})n_-(\mathbf{r}')] + 2U_{s,\text{inter}}(\mathbf{r} - \mathbf{r}') n_+(\mathbf{r})n_-(\mathbf{r}') \\ &+ 2U_{sc,1}(\mathbf{r} - \mathbf{r}') [n_+(\mathbf{r})n_{c,+} + n_-(\mathbf{r})n_{c,-}] + 2U_{sc,2}(\mathbf{r} - \mathbf{r}') [n_+(\mathbf{r})n_{c,-} + n_-(\mathbf{r})n_{c,+}] \\ &+ \kappa_{\text{surf}} U(\mathbf{r} - \mathbf{r}') [n_{c,+}n_{c,+} + n_{c,-}n_{c,-}] + 2U_{c,\text{inter}}(\mathbf{r} - \mathbf{r}') n_{c,-}n_{c,+} \}, \quad (\text{B3}) \end{aligned}$$

where the corresponding Coulomb potentials are

$$\begin{aligned} U(\mathbf{r}) &= \frac{e^2}{4\pi\epsilon_0\kappa_{\text{surf}}} \frac{1}{r}, \quad U_{s,\text{inter}}(\mathbf{r}) = \frac{e^2}{4\pi\epsilon_0\kappa_{\text{surf}}} \frac{1}{\sqrt{r^2 + 4l_z^2}}, \quad U_{sc,1}(\mathbf{r}) = \frac{e^2}{4\pi\epsilon_0\kappa_{\text{surf}}} \frac{1}{\sqrt{r^2 + |L_z - l_z|^2}}, \\ U_{sc,2}(\mathbf{r}) &= \frac{e^2}{4\pi\epsilon_0\kappa_{\text{surf}}} \frac{1}{\sqrt{r^2 + |L_z + l_z|^2}}, \quad U_{c,\text{inter}}(\mathbf{r}) = \frac{e^2}{4\pi\epsilon_0} \frac{1}{\sqrt{r^2 + 4L_z^2}}. \quad (\text{B4}) \end{aligned}$$

The physical meaning of Eq. (B3) is transparent. Its first term describes the standard Coulomb interaction of quasiparticles on the top and bottom surfaces of the TI slab. The second term corresponds to the intersurface interaction, therefore, $U_{s,\text{inter}}$ contains additional term $4l_z^2$ in the denominator compared to U . The second line in Eq. (B3) describes interactions of surface quasiparticles with the charge densities on the capacitor plates. The last line in Eq. (B3) does not depend on $n_\lambda(\mathbf{r})$ and is, therefore, irrelevant for the gap equations (obviously, this line describes the electrostatic interaction of charge densities on capacitor plates). The Fourier

transforms of interactions (B4) are given by

$$\begin{aligned} U(\mathbf{k}) &= \frac{e^2}{2\epsilon_0\kappa_{\text{surf}}} \frac{1}{k}, \quad U_{s,\text{inter}}(\mathbf{k}) = \frac{e^2}{2\epsilon_0\kappa_{\text{surf}}} \frac{e^{-2l_z k}}{k}, \quad U_{\text{sc},1}(\mathbf{k}) = \frac{e^2}{2\epsilon_0\kappa_{\text{surf}}} \frac{e^{-|L_z - l_z|k}}{k}, \\ U_{\text{sc},2}(\mathbf{k}) &= \frac{e^2}{2\epsilon_0\kappa_{\text{surf}}} \frac{e^{-|L_z + l_z|k}}{k}, \quad U_{c,\text{inter}}(\mathbf{k}) = \frac{e^2}{2\epsilon_0} \frac{e^{-2L_z k}}{k}, \end{aligned} \quad (\text{B5})$$

where $k = |\mathbf{k}|$. Further, it is convenient to rewrite the first term in Eq. (B3) as follows:

$$U(\mathbf{r} - \mathbf{r}') [n_+(\mathbf{r})n_+(\mathbf{r}') + n_-(\mathbf{r})n_-(\mathbf{r}')] = U(\mathbf{r} - \mathbf{r}') \Psi^\dagger(\mathbf{r}) \Psi(\mathbf{r}) \Psi^\dagger(\mathbf{r}') \Psi(\mathbf{r}') - 2U(\mathbf{r} - \mathbf{r}') n_+(\mathbf{r}) n_-(\mathbf{r}'). \quad (\text{B6})$$

The one-loop BK effective action [40] in the model under consideration reads as

$$\begin{aligned} \Gamma(G) &= -i \sum_{\lambda=\pm} \text{Tr}[\text{Ln}G_\lambda^{-1} + S_\lambda^{-1}G_\lambda - 1] + \frac{e^2}{2} \int d^3u \int d^3u' \left\{ \sum_{\lambda=\pm} \text{tr}[\gamma^0 G_\lambda(u, u') \gamma^0 G_\lambda(u', u)] D(u' - u) \right. \\ &\quad - \sum_{\lambda=\pm} \text{tr}[\gamma^0 G_\lambda(u, u)] \sum_{\lambda'=\pm} \text{tr}[\gamma^0 G_{\lambda'}(u', u')] D(u' - u) \\ &\quad + 2 \sum_{\lambda=\pm} \text{tr}[\mathcal{P}_+^\lambda \gamma^0 G_\lambda(u, u') \mathcal{P}_-^\lambda \gamma^0 G_\lambda(u', u)] [D_{s,\text{inter}}(u' - u) - D(u' - u)] \\ &\quad - 2 \sum_{\lambda=\pm} \text{tr}[\mathcal{P}_+^\lambda \gamma^0 G_\lambda(u, u)] \sum_{\lambda'=\pm} \text{tr}[\mathcal{P}_-^{\lambda'} \gamma^0 G_{\lambda'}(u', u')] [D_{s,\text{inter}}(u' - u) - D(u' - u)] \\ &\quad + 2 \sum_{\lambda=\pm} \text{tr}[\mathcal{P}_+^\lambda \gamma^0 G_\lambda(u, u) n_{c,+} + \mathcal{P}_-^\lambda \gamma^0 G_\lambda(u, u) n_{c,-}] D_{\text{sc},1}(u' - u) \\ &\quad + 2 \sum_{\lambda=\pm} \text{tr}[\mathcal{P}_+^\lambda \gamma^0 G_\lambda(u, u) n_{c,-} + \mathcal{P}_-^\lambda \gamma^0 G_\lambda(u, u) n_{c,+}] D_{\text{sc},2}(u' - u) - [n_{c,+} n_{c,+} + n_{c,-} n_{c,-}] \kappa_{\text{surf}} D(u' - u) \\ &\quad \left. - 2n_{c,+} n_{c,-} D_{c,\text{inter}}(u' - u) \right\} - \frac{G_{\text{int}}}{2} \int d^3u \sum_{\lambda=\pm} (\text{tr}[\gamma^0 G_\lambda(u, u)] \text{tr}[\gamma^0 G_\lambda(u, u)] - \text{tr}[\gamma^0 G_\lambda(u, u) \gamma^0 G_\lambda(u, u)]), \end{aligned} \quad (\text{B7})$$

where $\mathcal{P}_\pm^\lambda = (1 \pm \lambda)/2$ are the surface projectors. The trace in the first term is taken in the functional sense, the trace in the rest of terms is taken over spinor indices.

The extremum of the effective action $\frac{\delta\Gamma(G)}{\delta G_\lambda} = 0$ defines the following Schwinger-Dyson equation for the full fermion propagator:

$$\begin{aligned} iG_\lambda^{-1}(u, u') &= iS_\lambda^{-1}(u, u') - e^2 \left\{ \gamma^0 G_\lambda(u, u') \gamma^0 D(u' - u) - \gamma^0 \sum_{\lambda=\pm} \text{tr}[\gamma^0 G_\lambda(u, u)] \delta^3(u - u') \tilde{D}(0) \right. \\ &\quad \left. - \gamma^0 \text{tr}[\gamma^0 G_{-\lambda}(u, u)] \delta^3(u - u') [\tilde{D}_{s,\text{inter}}(0) - \tilde{D}(0)] + \gamma^0 n_{c,\lambda} \delta^3(u - u') \tilde{D}_{\text{sc},1}(0) + \gamma^0 n_{c,-\lambda} \delta^3(u - u') \tilde{D}_{\text{sc},2}(0) \right\} \\ &\quad - G_{\text{int}} \{ \gamma^0 G_\lambda(u, u) \gamma^0 - \gamma^0 \text{tr}[\gamma^0 G_\lambda(u, u)] \} \delta^3(u - u'), \end{aligned} \quad (\text{B8})$$

where the contribution due to the third term in the curly brackets in Eq. (B7) is zero because the fermion propagator of the full model is diagonal in surface indices. The trace is taken over the spinor indices only, $\tilde{D}(0)$, $\tilde{D}_{s,\text{inter}}(0)$, $\tilde{D}_{\text{sc},1}(0)$, $\tilde{D}_{\text{sc},2}(0)$ are the Fourier transforms of the corresponding interactions at zero momentum, and

$$D(u) \approx \delta(t) \frac{1}{4\pi\epsilon_0\kappa_{\text{surf}}} \int \frac{dk}{2\pi} J_0(kr), \quad (\text{B9})$$

where $J_0(kr)$ is the Bessel function. The overall neutrality condition (15) implies that the second term in the curly brackets in Eq. (B8) is equal to zero. The last two terms in the curly brackets for $n_{c,+} = -n_{c,-}$ (which stems from the symmetric charge distribution on the opposite surfaces of the slab) are equal to

$$[n_{c,\lambda} \tilde{D}_{\text{sc},1}(0) + n_{c,-\lambda} \tilde{D}_{\text{sc},2}(0)] = -\gamma^0 \frac{1}{2\epsilon_0\kappa_{\text{surf}}} n_{c,\lambda} [(L_z - l_z) - (L_z + l_z)] = n_{c,\lambda} \gamma^0 \frac{l_z}{\epsilon_0\kappa_{\text{surf}}}. \quad (\text{B10})$$

Notice the fact that the dependence on L_z cancels out in Eq. (B10). This means that the formalism correctly describes the TI slab in an applied external electric field. Thus, the gap equation (B8) takes the form

$$iG_\lambda^{-1}(u, u') = iS_\lambda^{-1}(u, u') - e^2 \left\{ \gamma^0 G_\lambda(u, u') \gamma^0 D(u' - u) - \gamma^0 \frac{l_z \delta^3(u - u')}{\epsilon_0 \kappa_{\text{surf}}} [n_{-\lambda} + n_{c, -\lambda}] \right\} - G_{\text{int}} \{ \gamma^0 G_\lambda(u, u) \gamma^0 - \gamma^0 \text{tr}[\gamma^0 G_\lambda(u, u)] \} \delta^3(u - u'). \quad (\text{B11})$$

The last term in the first curly brackets has a clear physical meaning. It describes a superposition of electric fields due to the capacitor plates and charged surfaces of the TI. Taking into account condition (5), i.e., $n_\lambda = -\lambda \epsilon_0 \mathcal{E} / e$, we conclude that the corresponding term in the gap equation (B8) vanishes and the gap equation takes the following final form:

$$iG_\lambda^{-1}(u, u') = iS_\lambda^{-1}(u, u') - e^2 \gamma^0 G_\lambda(u, u') \gamma^0 D(u' - u) - G_{\text{int}} \{ \gamma^0 G_\lambda(u, u) \gamma^0 - \gamma^0 \text{tr}[\gamma^0 G_\lambda(u, u)] \} \delta^3(u - u').$$

It is worth noting that we are working in the grand canonical ensemble. The corresponding free-energy density is expressed through the effective action Γ as $\Omega = -\Gamma/(VT)$, where VT is a $(2 + 1)$ space-time volume. On the solution of the gap equation (12B), we have the following surface free-energy density (compare with Appendix C in Ref. [45]):

$$\Omega_\lambda = -\frac{1}{8\pi l^2} [1 - 2n_F(\Delta_{\text{eff}, \lambda})] [\Delta_{\text{eff}, \lambda} + \mu_\lambda^{(0)} + s_B m^{(0)}] - \frac{1}{4\pi l^2} \sum_{n=1}^{\infty} \left\{ (\mu_\lambda^{(0)} + \mu_{n, \lambda}) [n_F(M_n - \mu_{n, \lambda}) - n_F(M_n + \mu_{n, \lambda})] + \frac{2M_n^2 + m_{n, \lambda}(m^{(0)} - m_{n, \lambda})}{M_n} [1 - n_F(M_n + \mu_{n, \lambda}) - n_F(M_n - \mu_{n, \lambda})] \right\} - \frac{\epsilon_0 \mathcal{E}^2}{2\kappa_{\text{surf}}} (\kappa_{\text{surf}} L_z - l_z), \quad (\text{B12})$$

where the last term has a transparent physical meaning and represents the energy density of an electric field outside the slab.

APPENDIX C: KERNEL COEFFICIENTS $\mathcal{K}_{m,n}^{(0)}$

In this appendix, we give the definition for the kernel coefficients $\mathcal{K}_{m,n}^{(0)}$ used in Coulomb part of the gap equation in the static approximation. Further, we provide an explicit expression for those coefficients in the case without polarization effects. The kernel coefficients are defined by [39]

$$\mathcal{K}_{m,n}^{(0)} = \int_0^\infty \frac{dk}{2\pi} \frac{kl \mathcal{L}_{m,n}^{(0)}(kl)}{k + \Pi(0, k)}, \quad (\text{C1})$$

$$\mathcal{L}_{m,n}^{(0)} = \frac{1}{l^2} \int_0^\infty dr r e^{-\frac{r^2}{2l^2}} L_m^0\left(\frac{r^2}{2l^2}\right) L_n^0\left(\frac{r^2}{2l^2}\right) J_0(kr) = (-1)^{m+n} e^{-\frac{k^2 l^2}{2}} L_m^{n-m}\left(\frac{k^2 l^2}{2}\right) L_n^{m-n}\left(\frac{k^2 l^2}{2}\right), \quad (\text{C2})$$

where we used formula 7.422.2 in Ref. [52] in order to perform the integration in Eq. (C2).

By neglecting the polarization effects, i.e., setting $\Pi(0, k) = 0$, and using formula 2.19.14.15 in Ref. [53], one obtains the following explicit result:

$$\mathcal{K}_{m,n}^{(0)} \Big|_{\Pi \rightarrow 0} = \int_0^\infty \frac{dx}{2\pi} \int_0^\infty dt e^{-t} L_m^0(t) L_n^0(t) J_0(x\sqrt{2t}) = \frac{\Gamma(n + 1/2) \Gamma(m + 1/2)}{2\sqrt{2} \pi^{3/2} m! n!} {}_3F_2(-m, -n, 1/2; 1/2 - m, 1/2 - n; 1), \quad (\text{C3})$$

where ${}_3F_2$ is the hypergeometric function.

-
- [1] X.-L. Qi and S.-C. Zhang, *Rev. Mod. Phys.* **83**, 1057 (2011).
[2] M. Z. Hasan and C. L. Kane, *Rev. Mod. Phys.* **82**, 3045 (2010).
[3] M. Z. Hasan and J. E. Moore, *Annu. Rev. Condens. Matter Phys.* **2**, 55 (2011).
[4] Y. Ando, *J. Phys. Soc. Jpn.* **82**, 102001 (2013).
[5] J. E. Moore and L. Balents, *Phys. Rev. B* **75**, 121306(R) (2007).
[6] C. L. Kane and E. J. Mele, *Phys. Rev. Lett.* **95**, 146802 (2005); **95**, 226801 (2005).
[7] D. Hsieh, Y. Xia, L. Wray, D. Qian, A. Pal, J. H. Dil, J. Osterwalder, F. Meier, G. Bihlmayer, C. L. Kane, Y. S. Hor, R. J. Cava, and M. Z. Hasan, *Science* **323**, 919 (2009).
[8] A. H. Castro Neto, F. Guinea, N. M. R. Peres, K. S. Novoselov, and A. K. Geim, *Rev. Mod. Phys.* **81**, 109 (2009).
[9] D. Hsieh, D. Qian, L. Wray, Y. Xia, Y. S. Hor, R. J. Cava, and M. Z. Hasan, *Nature (London)* **452**, 970 (2008).
[10] H. Zhang, C.-X. Liu, X.-L. Qi, X. Dai, Z. Fang, and S.-C. Zhang, *Nat. Phys.* **5**, 438 (2009).
[11] Y. L. Chen, J. G. Analytis, Z. H. Chu, Z. K. Liu, S. K. Mo, X. L. Qi, H. J. Zhang, D. H. Lu, X. Dai, Z. Fang, S. C. Zhang, I. R. Fisher, Z. Hussain, and Z. X. Shen, *Science* **325**, 178 (2009).
[12] Y. Xia, D. Qian, D. Hsieh, L. Wray, A. Pal, H. Lin, A. Bansil, D. Grauer, Y. S. Hor, R. J. Cava, and M. Z. Hasan, *Nat. Phys.* **5**, 398 (2009).

- [13] P. Roushan, J. Seo, C. V. Parker, Y. S. Hor, D. Hsieh, D. Qian, A. Richardella, M. Z. Hasan, R. J. Cava, and A. Yazdani, *Nature (London)* **460**, 1106 (2009).
- [14] T. Zhang, P. Cheng, X. Chen, J.-F. Jia, X. Ma, K. He, L. Wang, H. Zhang, X. Dai, Z. Fang, X. Xie, and Q.-K. Xue, *Phys. Rev. Lett.* **103**, 266803 (2009).
- [15] X.-L. Qi, T. L. Hughes, and S.-C. Zhang, *Phys. Rev. B* **78**, 195424 (2008).
- [16] L. Fu and C. L. Kane, *Phys. Rev. B* **76**, 045302 (2007).
- [17] Y. Xu, I. Miotkowski, C. Liu, J. Tian, H. Nam, N. Alidoust, J. Hu, C.-K. Shih, M. Z. Hasan, and Y. P. Chen, *Nat. Phys.* **10**, 956 (2014).
- [18] A. A. Koulakov, M. M. Fogler, and B. I. Shklovskii, *Phys. Rev. Lett.* **76**, 499 (1996).
- [19] Y. Ran, H. Yao, and A. Vishwanath, [arXiv:1003.0901](https://arxiv.org/abs/1003.0901).
- [20] B. I. Halperin, P. A. Lee, and N. Read, *Phys. Rev. B* **47**, 7312 (1993).
- [21] E. H. Rezayi and F. D. M. Haldane, *Phys. Rev. Lett.* **84**, 4685 (2000).
- [22] D. T. Son, *Phys. Rev. X* **5**, 031027 (2015).
- [23] S. D. Geraedts, M. P. Zaletel, R. S. K. Mong, M. A. Metlitski, A. Vishwanath, and O. I. Motrunich, *Science* **352**, 197 (2016).
- [24] B. Seradjeh, J. E. Moore, and M. Franz, *Phys. Rev. Lett.* **103**, 066402 (2009).
- [25] D. K. Efimkin, Yu. E. Lozovik, and A. A. Sokolik, *Phys. Rev. B* **86**, 115436 (2012).
- [26] J. Linder, T. Yokoyama, and A. Sudbo, *Phys. Rev. B* **80**, 205401 (2009).
- [27] P. Cea, *Eur. Phys. J. B* **89**, 104 (2016).
- [28] S.-Q. Shen, *Topological Insulators* (Springer, Berlin, 2012).
- [29] W.-Y. Shan, H.-Z. Lu, and S.-Q. Shen, *New J. Phys.* **12**, 043048 (2010).
- [30] E. Mooser and W. B. Pearson, *Phys. Rev.* **101**, 492 (1956).
- [31] J. Black, E. M. Conwell, L. Seigle, and C. W. Spencer, *J. Phys. Chem. Solids* **2**, 240 (1957).
- [32] Y.-S. Fu, T. Hanaguri, K. Igarashi, M. Kawamura, M. S. Bahramy, and T. Sasagawa, *Nat. Commun.* **7**, 10829 (2016).
- [33] T. W. Appelquist, M. Bowick, D. Karabali, and L. C. R. Wijewardhana, *Phys. Rev. D* **33**, 3704 (1986).
- [34] F. D. M. Haldane, *Phys. Rev. Lett.* **61**, 2015 (1988).
- [35] T. W. Appelquist, M. J. Bowick, D. Karabali, and L. C. R. Wijewardhana, *Phys. Rev. D* **33**, 3774 (1986).
- [36] Bismuth Selenide (Bi_2Se_3) Optical Properties, Dielectric Constants, in *Non-tetrahedrally Bonded Elements and Binary Compounds I*, edited by O. Madelung, U. Rossler, and M. Schulz (Springer, Berlin, 1998).
- [37] D. C. Elias, R. V. Gorbachev, A. S. Mayorov, S. V. Morozov, A. A. Zhukov, P. Blake, L. A. Ponomarenko, I. V. Grigorieva, K. S. Novoselov, F. Guinea, and A. K. Geim, *Nat. Phys.* **7**, 701 (2011).
- [38] J. Gonzalez, F. Guinea, and M. A. H. Vozmediano, *Nucl. Phys. B* **424**, 595 (1994).
- [39] E. V. Gorbar, V. P. Gusynin, V. A. Miransky, and I. A. Shovkovy, *Phys. Scr.* **T146**, 014018 (2012).
- [40] G. Baym and L. P. Kadanoff, *Phys. Rev.* **124**, 287 (1961); J. M. Cornwall, R. Jackiw, and E. Tomboulis, *Phys. Rev. D* **10**, 2428 (1974).
- [41] E. V. Gorbar, V. P. Gusynin, and V. A. Miransky, *Phys. Rev. B* **81**, 155451 (2010).
- [42] E. V. Gorbar, V. P. Gusynin, V. A. Miransky, and I. A. Shovkovy, *Phys. Rev. B* **66**, 045108 (2002).
- [43] V. P. Gusynin, V. A. Miransky, and I. A. Shovkovy, *Phys. Rev. Lett.* **73**, 3499 (1994).
- [44] V. A. Miransky and I. A. Shovkovy, *Phys. Rep.* **576**, 1 (2015).
- [45] E. V. Gorbar, V. P. Gusynin, V. A. Miransky, and I. A. Shovkovy, *Phys. Rev. B* **78**, 085437 (2008).
- [46] M. O. Goerbig, *Rev. Mod. Phys.* **83**, 1193 (2011).
- [47] R. Jackiw and C. Rebbi, *Phys. Rev. D* **13**, 3398 (1976).
- [48] Y. Baum and A. Stern, *Phys. Rev. B* **85**, 121105(R) (2012).
- [49] C. J. Tabert and J. P. Carbotte, *Phys. Rev. B* **92**, 245414 (2015).
- [50] T. W. Appelquist, D. Nash, and L. C. R. Wijewardhana, *Phys. Rev. Lett.* **60**, 2575 (1988).
- [51] H. Bateman and A. Erdelyi, *Higher Transcendental Functions*, Vol. 1 (McGraw-Hill, New York, 1953).
- [52] I. S. Gradshteyn and I. M. Ryzhik, *Tables of Integrals, Series, and Products* (Academic, Orlando, 1980).
- [53] A. P. Prudnikov, Yu. A. Brychkov, and O. I. Marichev, *Integrals and Series: Special Functions*, Vol. 2 (Nauka, Moscow, 1983).